

Measurements and Computations of the Turbulent Corner Flow on the NASA Juncture-Flow Model with a Symmetric Wing

Michael A. Kegerise*, Andrew N. Leidy†, Judith A. Hannon‡ and Christopher L. Rumsey§

NASA Langley Research Center, Hampton, VA 23681

Thomas H. Pulliam¶

NASA Ames Research Center, Moffett Field, CA 94035

The NASA Juncture Flow experiment is designed to acquire high-quality flowfield data deep in the corner of a wing-fuselage junction specifically for the purpose of computational fluid dynamics (CFD) validation and turbulence model improvement. This paper presents and discusses the results of a recent experiment with the juncture-flow model in the NASA Langley 14- by 22-Foot Subsonic Tunnel. The main objective of the test was to expand the existing juncture-flow dataset with a symmetric wing case that displays fully attached, incipient separation, and separated flow in the corner of the wing-fuselage junction, depending on the model angle of incidence. Laser Doppler velocimetry (LDV) measurements were made at three model angles of incidence (0° : fully attached, 1° : incipient separation, and 5° : separated flow) and for each one, mean-flow and Reynolds-stress data were obtained on the fuselage and at several streamwise locations along the corner of the wing-fuselage junction. Supporting measurements were made during the test campaign and included model and tunnel wall static pressures, tunnel wall and ceiling boundary-layer rake data, oil-flow visualizations, and laser-based measurements of the as-built model geometry and model position in the test section. Comparisons between the experimental data on the test article and Reynolds-averaged Navier-Stokes CFD results are presented and discussed.

Nomenclature

| | |
|-------------|---|
| c | chord length at wing planform break, 580.716 mm |
| c_f | skin-friction coefficient |
| C_p | surface pressure coefficient |
| c_r | chord length at wing root, 1052.8 mm |
| H | boundary layer shape factor |
| ℓ_v | viscous length scale, μm |
| M | Mach number |
| Q | dynamic pressure, Pa |
| R_a | roughness average, μm |
| Re_c | Reynolds number based on chord length at wing planform break |
| Re_θ | Reynolds number based on momentum thickness |
| R_q | roughness rms, μm |
| T_a | ambient temperature, K |
| U | velocity, m/s |
| u_i | (u_1, u_2, u_3) Cartesian velocity components (u, v, w), m/s |
| u'_i | (u'_1, u'_2, u'_3) velocity fluctuation (u', v', w'), m/s |
| x_i | (x_1, x_2, x_3) Cartesian coordinates (x, y, z), m (mm where noted) |

*Research Scientist, Flow Physics and Control Branch, M.S. 170.

†Research Aerospace Engineer, Flow Physics and Control Branch, M.S. 170.

‡Aerospace Engineer, Flow Physics and Control Branch, M.S. 170.

§Research Scientist, Computational Aerosciences Branch, M.S. 128.

¶Retired Senior Research Scientist.

| | |
|-----------------|--|
| α | angle of incidence, deg |
| δ | boundary-layer thickness, mm |
| δ^* | displacement thickness, mm |
| θ | momentum thickness, mm |
| Π | wake-strength parameter |
| ω_i | ($\omega_1, \omega_2, \omega_3$) Cartesian vorticity components ($\omega_x, \omega_y, \omega_z$), s^{-1} |
| $(\bar{\cdot})$ | mean value |

Subscript

| | |
|-----|-----------|
| ref | reference |
|-----|-----------|

I. Introduction

JUNCTION flows, such as those formed around a wing-fuselage or a wing-pylon intersection, often exhibit regions of flow separation that can adversely impact aircraft performance. For wing-fuselage junction flows, separation in the turbulent corner-flow region near the wing trailing edge can impact the maximum lift coefficient and may also significantly modify the stall characteristics of an aircraft.¹ As such, there is a strong desire to predict the onset and progression of separation reliably and accurately for this flow, but that remains a challenge for computational fluid dynamics (CFD) methods. To address that, NASA has developed a CFD validation experiment for a generic full-span wing-fuselage junction model that experiences corner-flow separation at subsonic flow conditions.^{2–5} In the present context, “CFD validation experiment” refers to the overall combined CFD/experimental effort necessary to produce validation-quality data.⁶ A primary goal of this effort was to provide high-quality flowfield data in the turbulent corner-flow region of the junction suitable for CFD validation and turbulence model improvements. To that end, significant resources were also focused on the collection of data for boundary conditions, model geometry, and uncertainty quantification—all of which allows for an unambiguous comparison of the flowfield data to the CFD simulations.

Two test campaigns with the NASA Juncture Flow (JF) model were previously conducted in the NASA Langley 14- by 22-Foot Subsonic Tunnel (14x22).^{3,5} There, the JF model was configured with a truncated F6 wing, which is a cambered wing design for a generic twin engine wide body aircraft.⁷ This configuration experienced corner-flow separation near the trailing edge of the wing-fuselage junction, with the onset location moving upstream with increasing model angle of incidence. Furthermore, corner-flow separation occurred for all angles of incidence considered, from -10° to $+10^\circ$. During these test entries, mean velocity and turbulent flowfield data were collected at selected locations on the model fuselage and in the corner-flow region of the wing-fuselage junction using internally mounted laser Doppler velocimetry (LDV) systems. A companion set of flowfield data in the corner-flow region was also collected with an internally mounted particle image velocimetry (PIV) system.^{5,8} In addition to the flowfield measurements, static and dynamic pressures were measured at selected locations on the model, infrared imaging was used to characterize boundary-layer transition, and oil flow was used to visualize the separated flow in the corner-flow region of the wing-fuselage junction. The as-built geometry and position of the model in the test section were measured via laser-based scanning techniques over the course of both test entries. Boundary conditions in the form of tunnel-wall pressures, diffuser pressures, and boundary-layer rake pressures were acquired and in an earlier test entry in the 14x22, the test section inflow conditions were documented using various measurement techniques.⁹ All of the data from these test campaigns are available on the NASA Langley Turbulence Modeling Resource (TMR) website.¹⁰

Comparisons with our JF measurements to date have shown that Reynolds-averaged Navier-Stokes (RANS) CFD methods used in conjunction with a linear eddy viscosity model tend to dramatically overpredict the size of the corner-flow separation. This is primarily due to the inability of linear models to correctly predict the anisotropy in the Reynolds normal-stress components in the corner-flow region. That anisotropy is responsible for the production of streamwise vorticity in the corner-flow region,¹¹ which acts to delay the onset of corner-flow separation in our case. RANS CFD methods used in conjunction with nonlinear eddy viscosity models—such as Spalart-Allmaras (SA) with rotation-curvature (RC) correction and the quadratic constitutive relation (QCR2000 or QCR2013)—fared far better, but still overpredicted the size of the corner-flow separation by approximately 30%. As a direct result of comparisons between the JF flowfield measurements and RANS CFD methods, an improved version of the quadratic constitutive relation—QCR2020—was developed and this was found to provide better predictions of the normal-stress anisotropy and consequently, better predictions for the onset of corner-flow separation on the JF configuration.^{5,12}

The original goal of the JF CFD validation experiment was to test the juncture-flow model with a single wing configuration that displayed a progression from fully attached corner flow to a large corner-flow separation with increasing model angle of incidence. Early in the project, risk-reduction tests in the Virginia Tech Stability Tunnel¹³ and the 14x22¹⁴ were performed on smaller-scale models with several wing candidates, but none of them were found to display the desired behavior. The F6-based wing design did display a large corner-flow separation, but separation occurred for all the angles of incidence that were considered. A second wing configuration with a symmetric profile (based on NACA four-digit wing sections) did display a progression from fully attached corner flow to separated corner flow, but the size of the separated flow region remained very small. Since neither wing design was optimal in terms of our original goal, a decision was made to build both the F6 wing and the symmetric wing for the CFD validation experiment so that data for fully attached, incipient, and separated corner flow could be obtained.

As noted earlier, the F6 wing was the subject of two previous test entries in the 14x22. Recently, a third test campaign was conducted in the 14x22 with the symmetric wing configuration and there, the primary objective was to obtain flowfield data in the turbulent corner-flow region of the wing-fuselage junction. A secondary objective was to quantify the natural transition location on the fuselage and wing surfaces. In this paper, we present the details of third test entry related to the primary objective, present sample test results, and compare the experimental test results to RANS CFD simulations with SA-RC-QCR2020. The test details and results associated with measurements of natural transition on the JF model are reported separately in Leidy et al.¹⁵

II. Experimental Details

A. Wind-tunnel facility

The experiment was conducted in the NASA Langley 14- by 22-Foot Subsonic Tunnel, which is a closed-circuit, atmospheric-pressure wind tunnel capable of operating in an open, partially closed, or closed test-section mode. Measurements for this study were made in the closed test section mode and in that case, the test section measures approximately 4.42 m high by 6.63 m wide by 13 m long, and the maximum freestream velocity is 103 m/s. The turbulence intensity was between 0.07 and 0.08% at a dynamic pressure of 2.87 kPa, but that does vary somewhat with dynamic pressure and location in the test section.¹⁶ Further details about the tunnel can be found in Gentry et al.¹⁷

Table 1. Nominal test conditions and associated ranges.

| | Nominal value | Range |
|-----------------|------------------|---|
| Re_c | $2.4 \cdot 10^6$ | $\pm 0.25\%$ |
| M | 0.189 | [0.171, 0.199] |
| T_a , K | 288.84 | [281, 309] |
| U_{ref} , m/s | 64.4 | [57.5, 69.9] |
| Q , Pa | 2385 | [2071, 2725] |
| α , deg. | 0.0, 1.0, 5.0 | [-0.038, 0.031], [0.986, 1.028], [4.986, 5.031] |

Throughout all of the wind-tunnel runs, the tunnel controller held the chord Reynolds number, Re_c , at a constant value of $2.4 \cdot 10^6$ to within $\pm 0.25\%$. Since the facility does not have a temperature controller, the freestream velocity was adjusted to maintain a constant Re_c as the air temperature changed over the course of a given run and from day-to-day due to changes in the prevailing outdoor conditions. The nominal test conditions and their associated ranges over the course of the test entry are shown in Table 1.

B. Juncture-flow model

The JF model is a full-span wing-fuselage body with a modular design that can be configured with different fuselage nose sections and different wing designs. In addition, each wing design has a removable leading-edge insert at the root that allows the wing to be configured with or without a leading-edge root extension that mitigates the leading-edge horseshoe vortex of the wing-fuselage junction. The fuselage has flat side walls with six locations for instrumentation inserts (three on each flat side of the fuselage) that provide access to the fuselage nose section boundary layer, the fuselage boundary layer near the wing leading edge, and the wing-fuselage corner flow. For this test entry, the inserts were configured with either static-pressure ports or thin (1 mm) antireflection coated acrylic windows that provided

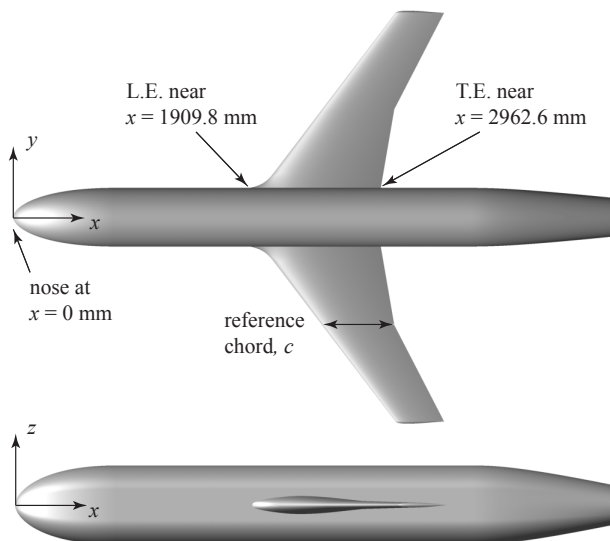


Figure 1. Top and side views of the wing-fuselage junction model geometry.

optical access for the LDV probes stowed within the model. All of the model parts were painted with a black lusterless polyurethane paint suitable for both infrared imaging and oil-flow visualizations on the model surface. The average roughness, R_a , and the rms roughness, R_q , for the painted model surface was $2.70 \pm 0.94 \mu\text{m}$ and $3.33 \pm 1.12 \mu\text{m}$, respectively.

For the present study, the JF model was configured with the shorter of two available fuselage nose sections (to date, the longer nose has not been used in any test), and symmetric wings with leading-edge root extensions. A top and side view of the model geometry for this configuration is shown in Fig. 1. The symmetric wing design is a blending of an NACA 0015 section at the root, an NACA 0012 section near the wing break, and an NACA 0010 section further outboard. The wing has a leading-edge sweep angle of 37.3° and a planform break located 869.7 mm from the model centerline. The planform break chord length, c , was 580.716 mm and this was used as the reference length for Re_c . The overall length, height and width of the fuselage for this configuration was 4.839 m, 0.630 m, and 0.472 m, respectively, and the tip-to-tip wing span was 3.327 m. A port-side view of the model installed in the 14x22 is shown in Fig. 2. Here, we see that the model is attached—via a long sting cannon—to a motorized sting mast that allows for adjustments to the model pitch and yaw angles, as well as the model height. The height adjustment allows for a reference point on the model (located 2.448 m from the model nose tip and on the fuselage centerline) to be kept near the center of the test section during a pitch-angle adjustment. In addition, the sting cannon was motorized for adjustments to the model roll angle. Both the pitch and roll angles were measured with a pair of accelerometer-based model-attitude sensors located inside the model fuselage.

To ensure a turbulent boundary layer on the fuselage and wing surfaces, commercially-produced trip-dot tape was used to fix the transition location. The trip dots were cylindrical with a diameter of 1.16 mm and a center-to-center spacing of 2.47 mm. On the fuselage, trip dots with a height of $289.4 \mu\text{m}$ were placed at a nominal distance of 336 mm from the fuselage nose tip. On the upper and lower wing surfaces, trip dots with a height of $218.4 \mu\text{m}$ were placed along the wing span at an arc distance from the leading edge equal to 6.4% of the local chord length. A second row with a height of $205.7 \mu\text{m}$ was placed on the outer 75% of the wing span at 1.6% of the local chord length. That row was used to eliminate a laminar separation bubble that was observed for model angles of incidence greater than 7° . Transition to turbulent flow via the trip-dot arrays was confirmed with infrared imaging of all model surfaces over angles of incidence ranging from -10° to $+10^\circ$.

C. Laser Doppler velocimetry measurements

Flowfield velocity measurements were made with a pair of miniature laser Doppler velocimetry (LDV) probes that were located inside the junction model, and each probe was mounted to a three-axis traverse system. One LDV probe was located near the wing trailing edge and was used to survey the wing-fuselage corner flow. The other LDV probe



Figure 2. Port-side view of the wing-fuselage junction model installed in the 14- by 22-Foot Subsonic Tunnel.

was alternately used to survey the boundary layer on the fuselage nose section, the fuselage boundary layer in the vicinity of the wing leading edge, and the wing-fuselage corner flow near the wing leading edge.

The LDV systems are a custom design comprised of a photonics system that provides laser light, a fiber-optic-based probe head with off-axis receiving optics, photomultipliers to detect Doppler bursts, and a data acquisition computer with a high-speed A/D board and burst-processing software. Details of this system were previously reported in Kegerise et al.³ and so here, we only present the salient features of the system. The LDV probe emits seven laser beams, five at a wavelength of 532 nm (green) and two at a wavelength of 488 nm (blue). The five green beams form three overlapping, frequency-shifted (-80, -200, and 350 MHz) measurement volumes with nominal diameter and length of 140 μm and 960 μm , respectively, at a working distance of 90 mm. The measurement directions defined by these three measurement volumes are nonorthogonal and depend on the probe-head orientation inside the model. Therefore, a linear transformation was developed to convert the measured velocity components to those in the orthogonal body-fixed coordinate system. To that end, each of the beam unit vectors were measured in situ and then used to calculate the measurement directions, the measurement volume fringe spacings, and the linear transformation.

The two blue beams form a frequency shifted (-200 MHz) measurement volume with a converging set of fringes along their bisector that overlaps the green beam measurement volumes. Using the Doppler-shifted frequency measured with this measurement volume and the velocity measured by the green beam measurement volumes (which have a uniform fringe spacing), the local fringe spacing of the blue beam measurement volume can be calculated. Then, using a simple linear model for the converging fringe pattern and the calculated fringe spacing, the position of the particle along the bisector of the measurement volume is calculated. When performing these calculations, only coincident data (i.e., from the same particle) measured with the blue- and green-beam measurement volumes is considered. A key advantage of this capability is that the particle positions can be used to achieve submeasurement-volume spatial resolution. Details on the theory and development of this particle-position-resolving capability can be found in Lowe^{18,19} and Brooks and Lowe.²⁰

Scattered light from the measurement volume was collected with a 110 mm focal length lens oriented at approximately 35° to the optical axis of the probe head and subsequently focused onto a multimode fiber with a diameter of 105 μm . With this off-axis arrangement, the effective length of the measurement volumes was approximately 180 μm .^a The multimode fiber was then connected to a pair of photomultipliers (PMTs), each fitted with a filter that passed either green or blue wavelengths. The amplified signals from the PMTs were sampled with an 8 bit, 1 GHz sample rate data acquisition card. Burst detection for each channel was performed in the time domain and Doppler-shifted frequencies were extracted from the power-spectral densities of the sampled burst signals. Specific details on the burst-processing algorithm can be found in Lowe.¹⁸ For the blue channel burst signals, a single Doppler-shifted frequency associated with the measurement volume was present, while for the green channel burst signals, three Doppler-shifted frequencies—associated with the three measurement volumes—were present when coincidence was satisfied. For the green channel, the frequency shift for each measurement volume was separated far enough apart in the frequency domain so that no signal ambiguity could occur for our flow conditions.

Seeding for the LDV measurements was provided by a smoke generator that uses a low-residue mineral oil and

^aAs a point of reference, this is approximately 25 times the viscous length scale for the turbulent boundary layer on the fuselage nose section.

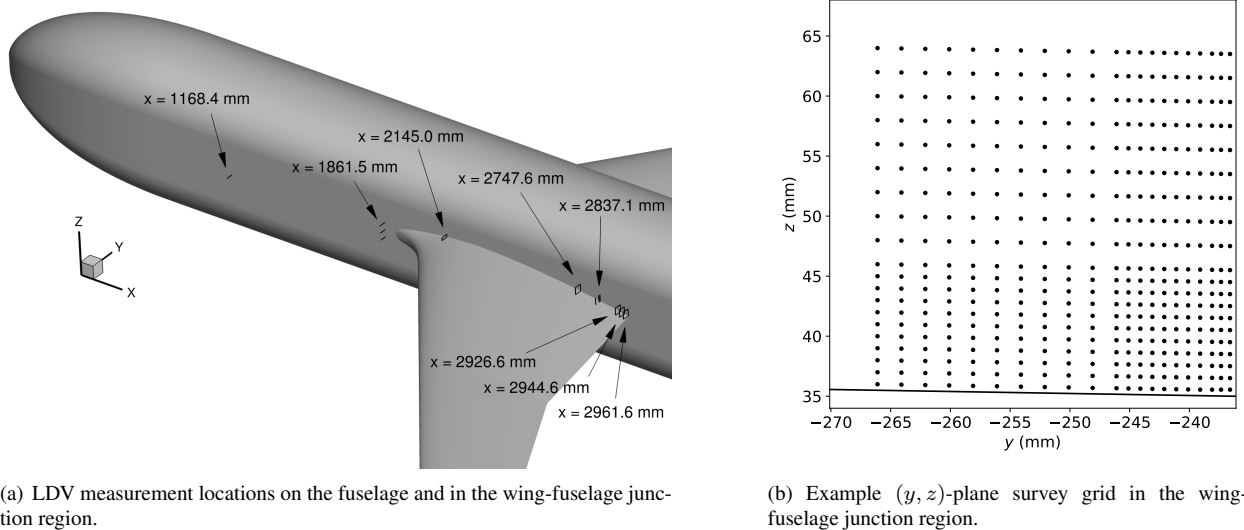


Figure 3. LDV measurement details.

produces a narrow distribution of particle sizes with a nominal diameter of $0.94 \mu\text{m}$. The smoke generator was placed in the wind tunnel settling chamber ahead of the honeycomb and was operated continuously during a wind-tunnel run so that adequate burst data rates were achieved. Depending on where the measurement volume was located in the flowfield, validated (i.e., coincidence was satisfied) burst data rates on the order of 100 to 500 bursts/s were typically observed.

For each spatial location in a flowfield survey, a fixed number of validated Doppler bursts were sampled and the measured Doppler-shifted frequencies from the three measurement volumes formed by the five green laser beams were used to calculate three nonorthogonal velocity components. The histograms of those velocity components were then calculated and the histogram-clipping routine of Ölçmen and Simpson²¹ was applied for removal of noise and outliers. The nonorthogonal velocity components were then transformed to orthogonal velocity components in the body-fixed coordinate system. Histograms of those components were calculated and once again, the histogram-clipping routine was applied. The processed velocity samples were then used to calculate several statistical moments, including the mean velocity components, the six independent components of the Reynolds-stress tensor, and all ten independent components of the velocity triple products. To account for velocity bias effects on the statistical moments, each sample was weighted by the particle transit time (or burst duration, which was recorded by the burst processor for each sample) through the measurement volume.²² Typically, 15,000 samples were used to calculate the statistical moments and for the data rates that were achieved (100 to 500 samples/s), many of the samples were statistically independent, being separated in time by at least two times the integral time scale.²²

Most of the LDV measurements were made with the LDV probes operated solely with the five green laser beams to obtain velocity measurements. For measurements on the fuselage nose section however, the LDV probe was operated with all seven lasers beams to measure both velocity and particle position. In that case, the measurement volume bisector was oriented normal to the fuselage window surface so that particle positions were measured in that direction. By making a series of closely-spaced and overlapping measurements in the wall-normal direction, a composite point cloud of particle position versus velocity was formed. The particle positions and associated velocity components were then divided into bins along the wall-normal direction, each with a width of $50 \mu\text{m}$, and statistical moments for the samples in each bin were calculated. This approach allowed for finer spatial resolution in the near-wall region of the fuselage boundary layer.

For a given model angle of incidence, LDV data were collected at several x locations on the port side of the JF model as depicted in Fig. 3a. On the fuselage, data were collected during wall-normal surveys at selected (x, z) locations. In the wing-fuselage corner region, data were primarily collected during (y, z) planar surveys, an example of which is shown in Fig. 3b. Here, the planar survey consisted of 420 measurement locations, with grid spacings ranging from 0.5 mm to 2 mm. Repeat (or replicate) measurements at all x locations were performed to aid in the development of uncertainty estimates. Three model angles of incidence were considered for the LDV measurements: 0° , 1° , and 5° , which correspond to fully attached, incipient, and separated corner flow as determined via oil-flow visualization

(see section IV.A for details).

The uncertainties in the instantaneous velocity components derived from the LDV measurements were estimated to be $U_u = 0.0065 \|\vec{u}\|$, $U_v = 0.0295 \|\vec{u}\|$, and $U_w = 0.0079 \|\vec{u}\|$, where $\|\vec{u}\|$ is the magnitude of the velocity vector.³ To estimate the uncertainties in the various statistical moments, a statistical analysis of residuals method, as described by Aeschliman and Oberkampf,²³ was employed. That involved comparisons of replicate measurements made over the course of the LDV data collection, which transpired over a period of days to several weeks. Replicate measurements made at the same nominal Reynolds number, model angle of incidence, test-section location, and flowfield location yielded information about the random component of uncertainty. Replicate measurements made before and after a physical repositioning of the LDV hardware, which required a remeasurement of the probe beam unit vectors, yielded information about that effect on the measurement uncertainty. Combining both factors, the statistical analysis of residuals yielded a three-standard-deviation (99.7% confidence interval) uncertainty estimate for each point in a flowfield survey.

D. Supplementary measurements

The JF model was instrumented with 244 static pressure ports on the fuselage and 289 static pressure ports on the symmetric wings. Electronically scanned pressure (ESP) modules, which were stowed in the JF model, were used to measure the mean pressure at each port. The full-scale range of the modules was 6.89 kPa (1psid) or 34.47 kPa (5 psid) depending on the expected pressure range of the ports connected to the module, and the modules were referenced to the ambient pressure in the control room of the 14x22. Additional mean pressure measurements were made at static pressure ports on the ceiling, the port-side wall, and the starboard-side wall of the test section. The mean total pressures from a set of boundary-layer rakes mounted to the ceiling, the port-side wall, and the starboard-side wall were also acquired. The static pressure data were collected for model angles of incidence ranging from -10° to $+10^\circ$ in 2.5° increments, and with the model both upright and inverted. Given the port-starboard and top-bottom symmetry of the JF model, the fuselage static pressures from the port and starboard sides were combined into a single one-sided data set for each angle of incidence. Similarly for the wing, the port and starboard side data, along with the upright and inverted data, were combined into a single one-sided data set. For these combined data sets, the effects of any flow nonuniformity, flow angularity, and model geometric differences on the measurement uncertainty were captured. Note that the static pressure data on the JF model were not corrected for wall effects and do not include flow-angularity corrections.

Oil-flow visualizations near the trailing edge of the wing-fuselage junction were used to determine the model angles of incidence at which the corner flow was fully attached, near incipient separation, and separated. For the separated flow case, approximate measurements of the length and width of the corner-flow separation were used to guide the selection of x locations for the LDV measurements. The oil-flow material was a mixture of 1 part titanium dioxide (TiO_2), 2 parts kerosene, and 0.3 parts oleic acid.

An in situ (in tunnel, wind off) measurement of the as-built JF model geometry was made with a laser-based, portable coordinate measurement machine (CMM) that has a quoted accuracy of 0.1 mm. In addition, Geographic Information System (GIS) scans provided lower fidelity measurements of the JF model, sting mast, and sting positions in the test section for each model angle of incidence at which LDV measurements were performed. Further details on and discussion of the geometry scans can be found on the NASA TMR website.¹⁰

III. Numerical Methods

The NASA FUN3D code^{24,25} was used for all computations in this paper. FUN3D is an unstructured three-dimensional, implicit, Navier-Stokes code that is nominally second-order spatially accurate. Roe's flux difference splitting²⁶ was employed. Other details regarding the code can be found in the extensive bibliography that is accessible at the FUN3D website.²⁷

The RANS computations here were all performed in "free air" (tunnel walls were not accounted for). Previous JF studies have looked at the influence of tunnel walls on CFD results.^{28,29} Although quantifiable, the wall effects on most of the JF flowfield quantities of interest were relatively small. In the current free-air studies, a farfield Riemann invariant boundary condition was imposed on the outer boundary, no-slip solid wall boundary conditions were applied on the test article, and symmetry conditions were used on the x - z symmetry plane. The default turbulence model employed was Spalart-Allmaras³⁰ with Rotation-Curvature correction³¹ and QCR2020¹² (SA-RC-QCR2020).

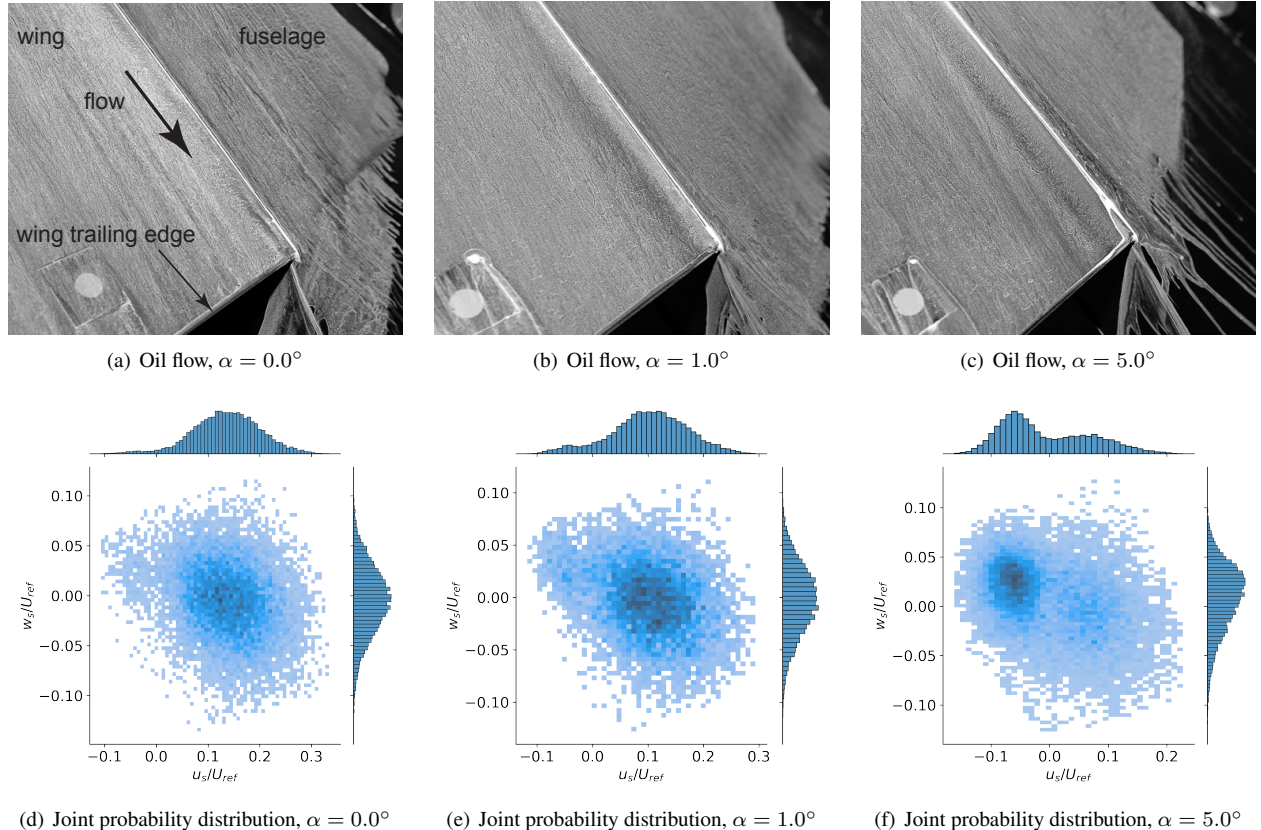


Figure 4. Oil-flow visualizations near the trailing edge of the wing-fuselage junction and joint probability distributions for velocity components tangential (u_s/U_{ref}) and normal (w_s/U_{ref}) to the wing surface at $x = 2961.6$ mm and $(\Delta y, \Delta z) = (500 \mu\text{m}, 500 \mu\text{m})$ from the junction corner.

IV. Results

In this section, a sampling of the experimental data is presented, along with some comparisons to RANS CFD. The full set of data for the test entry can be found on the NASA TMR website.¹⁰

A. Surface visualizations in the wing-fuselage junction region

Oil-flow visualizations of the corner flow near the wing trailing edge are shown for several model angles of incidence in Figs. 4a–c. At $\alpha = 0^\circ$ (Fig. 4a), the oil flow suggests that the corner flow is fully attached and no back flow of the oil-flow material was observed. At $\alpha = 1^\circ$ (Fig. 4b), the oil-flow again suggests fully attached corner flow, but it is on the verge of separating (which here, we define as incipient separation). With a slight increase in α to 1.25° (not shown), oil-flow material began to accumulate in the corner, signaling the formation of a separated-flow region with back flow. With further increases in α , a nodal point of separation in the wing-fuselage corner was observed to move upstream and a line of separation emanating from the nodal point was observed on the wing surface. Figure 4c shows the small corner-flow separation that forms at $\alpha = 5^\circ$. For this case, the separation length (defined as the straight line distance from the nodal point to the trailing edge) and width (defined as the distance along the trailing edge from the fuselage to the point where the separation line intersects the trailing edge) were 23.5 ± 3.7 mm and 3.5 ± 0.8 mm, respectively.

Since the oil-flow visualizations provide only a qualitative and time-averaged picture of the surface-flow topology, it was of interest to examine how velocity samples from LDV measurements very close to the junction corner correlate with the oil flow. To that end, Figs. 4d–f show the joint probability distributions for the velocity components tangential, u_s , and normal, w_s , to the wing surface at an x location 1 mm upstream from the trailing edge and $(\Delta y, \Delta z) = (500 \mu\text{m}, 500 \mu\text{m})$ from the corner. The probability density functions (PDF) for each of the components are also included on the top and right side of each plot. For $\alpha = 0^\circ$ (Fig. 4d), where the oil flow suggests fully-attached corner flow, the

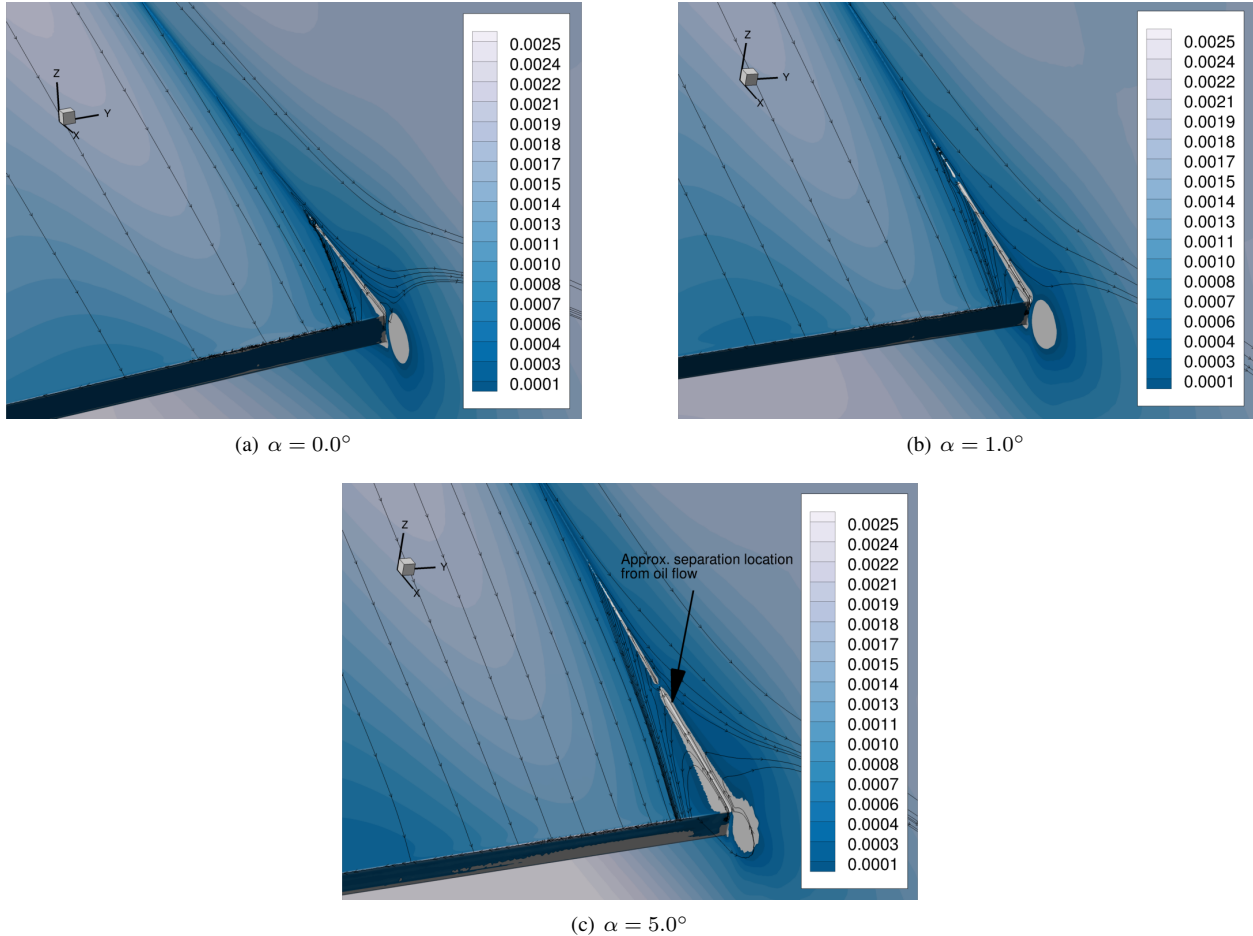


Figure 5. Skin-friction lines and contours of the x component of c_f computed with FUN3D for three angles of incidence. The gray contour level denotes regions where $c_{f,x} \leq 0$.

mean velocity vector points downstream, but the joint distribution indicates intermittent back flow approximately 3% of the time. Here, presumably, the mean-velocity magnitude is low enough such that large-scale turbulent structures in the corner flow boundary layers can induce an intermittent back flow near the corner. For $\alpha = 1^\circ$ (Fig. 4e), where the oil flow suggests incipient separation, the mean velocity vector still points downstream but is reduced in magnitude, and the joint distribution shows an increase in intermittent back flow to approximately 9% of the time. For $\alpha = 5^\circ$ (Fig. 4f), where the oil flow indicates a separated corner flow, the mean velocity vector now points upstream and the joint distribution indicates backflow 59% of the time. The bimodal nature of the joint distribution for this case—indicating intermittent forward and back flow—hints at the highly unsteady nature of the corner-flow separation.

Contours for the x component of the skin friction coefficient, $c_{f,x}$, and skin-friction lines computed with FUN3D (with SA-RC-QCR2020) are shown in Fig. 5. Here, the view is focused on the trailing-edge corner region and the gray contour level demarcates regions where $c_{f,x} \leq 0$. In contrast to the oil-flow visualizations, FUN3D predicts a separated flow region for all three angles of incidence. For $\alpha = 5^\circ$ (Fig. 5c), FUN3D predicts a separation length and width of 45.9 mm and 7.3 mm, respectively, which is roughly twice that observed in the oil flow. Although not shown here, other RANS turbulence models produced worse predictions. For example, the SA-RC-QCR2013-V model predicted a corner-flow surface topology unlike that displayed in the experiment and the SA-RC model predicted an even larger separation than SA-RC-QCR2020 for any given angle of incidence.

B. Model static pressures

For brevity, we will focus the discussion on the fully attached case at $\alpha = 0^\circ$ in the remaining sections of the paper. The static pressures and flowfield data for the other angles of incidence can be found on the NASA TMR website.¹⁰ Figure 6a shows the spanwise locations on the wing at which the static-pressure distributions were measured. Figures

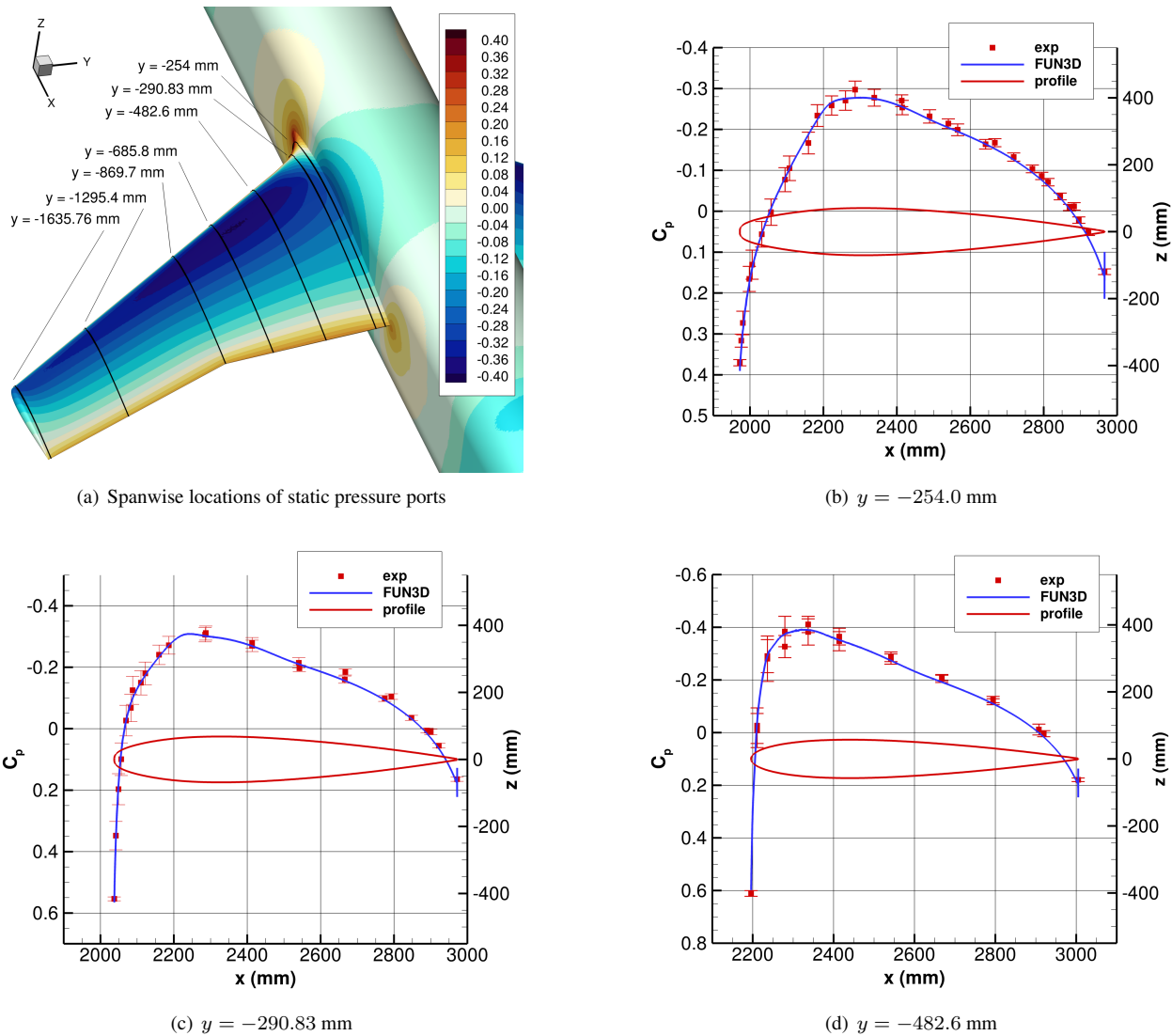


Figure 6. Surface pressure coefficients on inner part of wing, $\alpha = 0^\circ$.

6b-d and 7a-d show the resulting C_p distributions on the inner and outer parts of the wing span, respectively. Here, the C_p values are an average of the model upright and inverted data, as well as the port- and starboard-side data (except for the two most inboard stations where only the upright and inverted data from the starboard-side pressure ports were included in the average since there were no corresponding measurements on the port side). The average values are also comprised of several repeated measurements of the C_p values and the uncertainty bars represent a 95% confidence interval. The corresponding C_p distributions computed with FUN3D are also shown in the plots and they are in good agreement with the experimental data, generally being within the measurement uncertainty.

Figure 8a shows selected locations on the fuselage at which static-pressure distributions were measured and the corresponding C_p distributions are shown in Figs. 8b-f. For the C_p distributions in the y - z planes (Figs. 8c-f), the abscissa is the angle θ measured from the center of the fuselage with $\theta = -90^\circ$ representing the bottom of the fuselage and $\theta = 90^\circ$ representing the top. As with the wing pressure data, the measured C_p values represent the average of the port/starboard data, the upright/inverted data, and the repeated measurements. The corresponding C_p distributions computed with FUN3D are again found to be in good agreement with the experimental data.

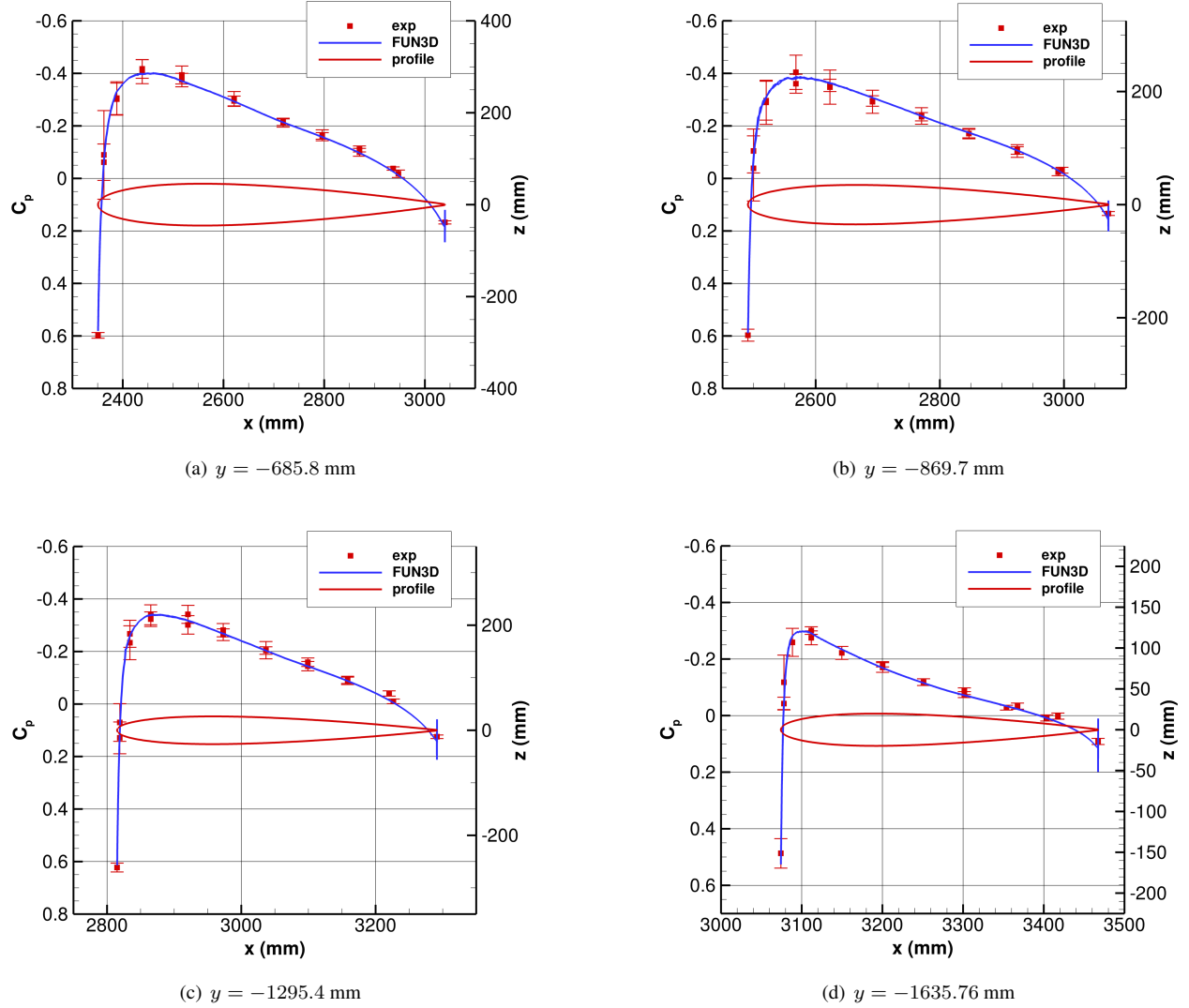
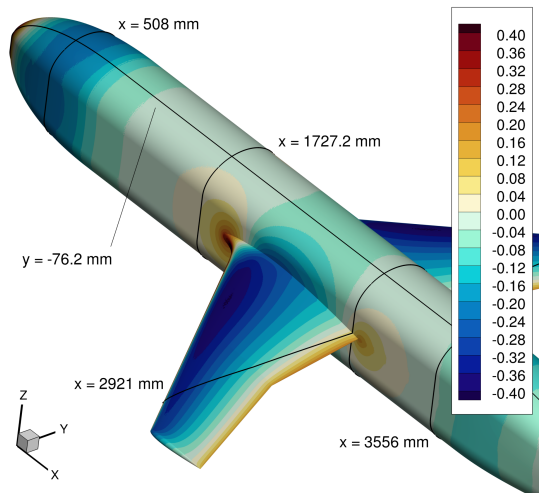


Figure 7. Surface pressure coefficients on outer part of wing, $\alpha = 0^\circ$ (see Fig. 6a).

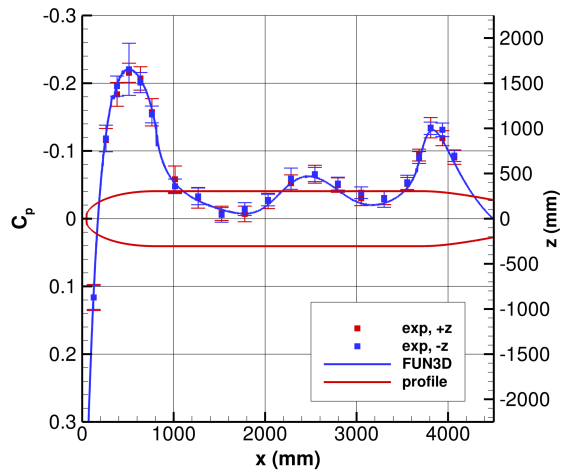
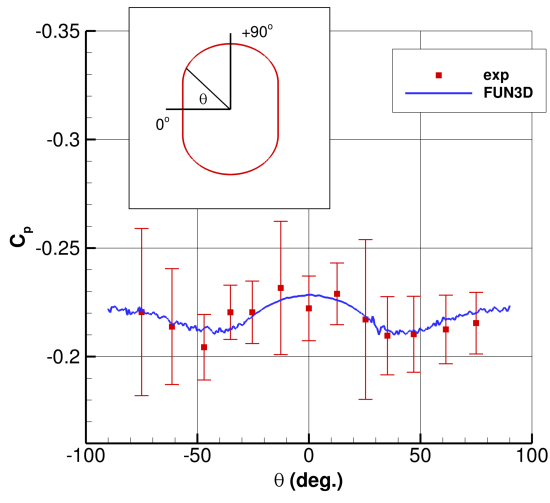
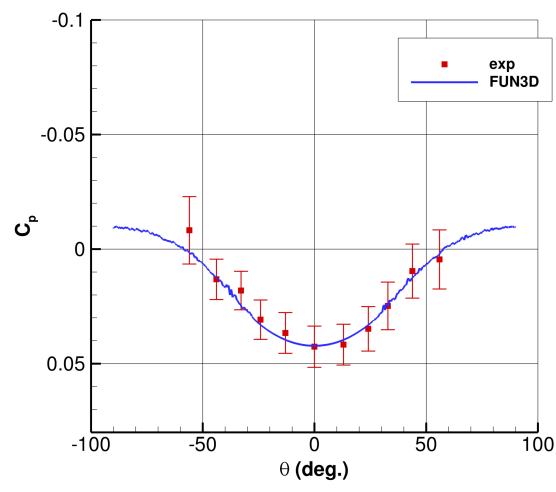
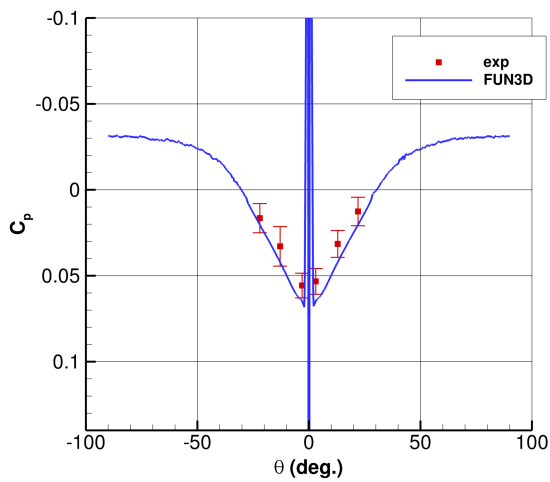
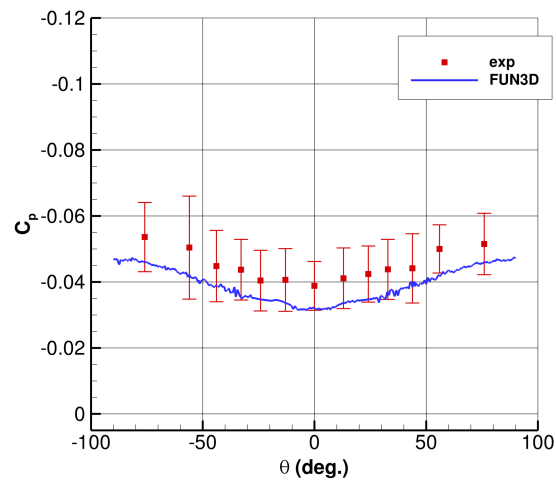
C. Mean-velocity and Reynolds-stress measurements on the fuselage

In this section we focus the discussion on a couple of boundary-layer profiles measured on the port side of the fuselage. To provide some context for the profile measurements, the computed surface pressure coefficient and skin-friction coefficient magnitude on the fuselage nose section are shown in Fig. 9. The first measurement location is at $x = 1168.4$ mm and $z = 0$ mm, which is far upstream of the wing-fuselage junction and on the symmetry plane of the flat fuselage side wall. Here, the C_p distribution indicates that the boundary layer is developing under a mild adverse pressure gradient in the streamwise direction. The second measurement location is at $x = 1861.5$ mm and $z = 0$ mm, which is just upstream of the wing-fuselage junction (≈ 48 mm) and here the boundary layer is developing under a stronger adverse pressure gradient. However, the flow in this region is still attached. As discussed earlier, transition on the fuselage was fixed in the experiment by a row of trip dots placed around the circumference of the fuselage at $x \approx 336$ mm. In the computations, however, the trip dots were not directly modeled. Rather, the transition location was imposed by zeroing out the production terms in the turbulence model ahead of the $x = 336$ mm location. Shortly downstream of that location, the computed boundary layer becomes fully turbulent and that is reflected by the sharp rise in the skin-friction coefficient observed in Fig. 9b.

The mean-velocity and Reynolds-stress profiles at the $x = 1168.4$ mm location, well upstream of the wing, are shown in Fig. 10a. Here, the shaded bands about the experimental data represent the measurement uncertainty and the solid lines denote the computed boundary layer profile quantities. For the abscissa label in the plots, y_o denotes the



(a) Locations of static pressure ports on fuselage

(b) $y = -76.2 \text{ mm}$ (c) $x = 508 \text{ mm}$ (d) $x = 1727.2 \text{ mm}$ (e) $x = 2921 \text{ mm}$ (f) $x = 3556 \text{ mm}$ Figure 8. Surface pressure coefficients on the fuselage, $\alpha = 0^\circ$.

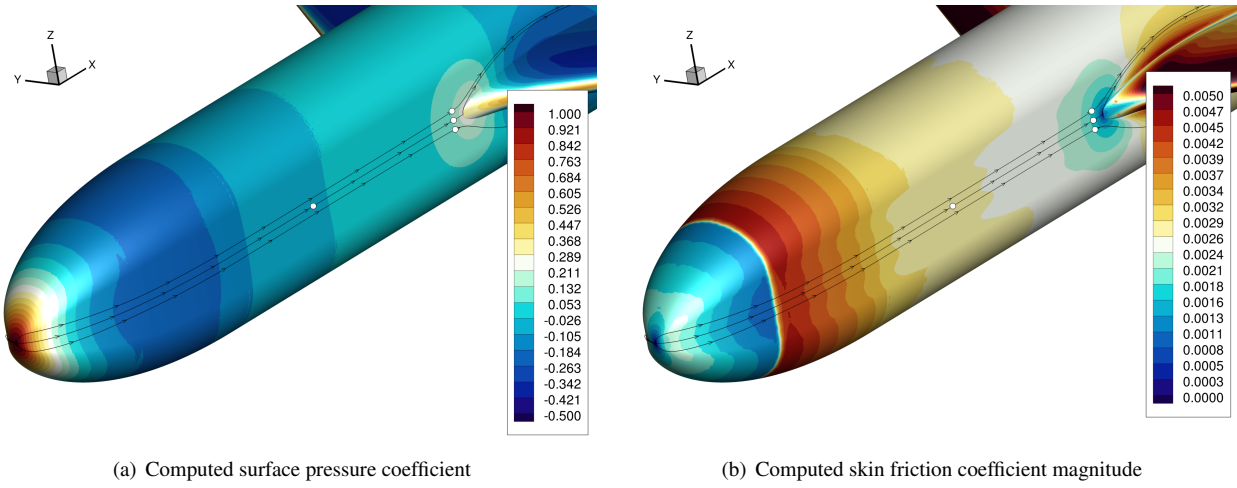


Figure 9. Computed surface contours of selected quantities at $\alpha = 0^\circ$. Skin-friction lines passing through the (x, z) -locations of the boundary layer profile measurements on the fuselage (filled circles) are also shown.

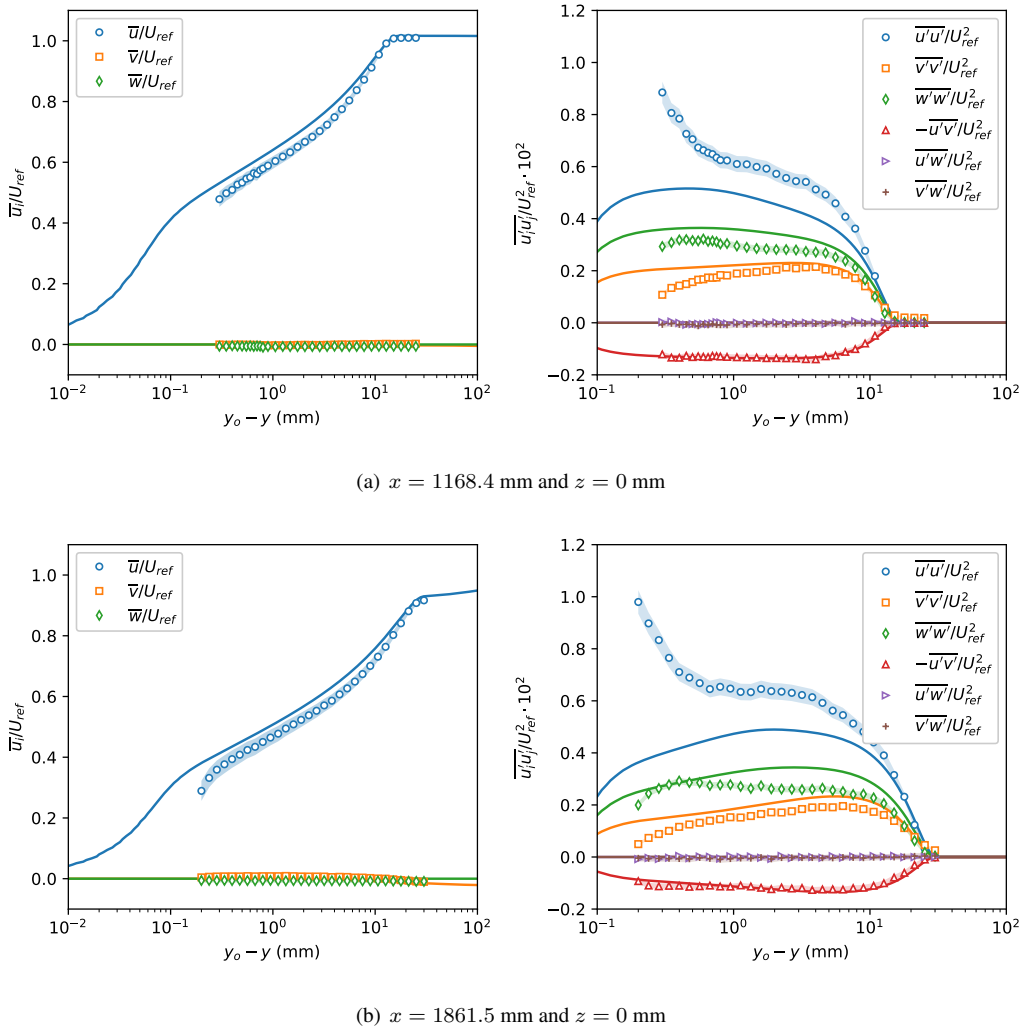


Figure 10. Measured (symbols) and computed (lines) mean-velocity and Reynolds-stress profiles on the fuselage at $\alpha = 0^\circ$.

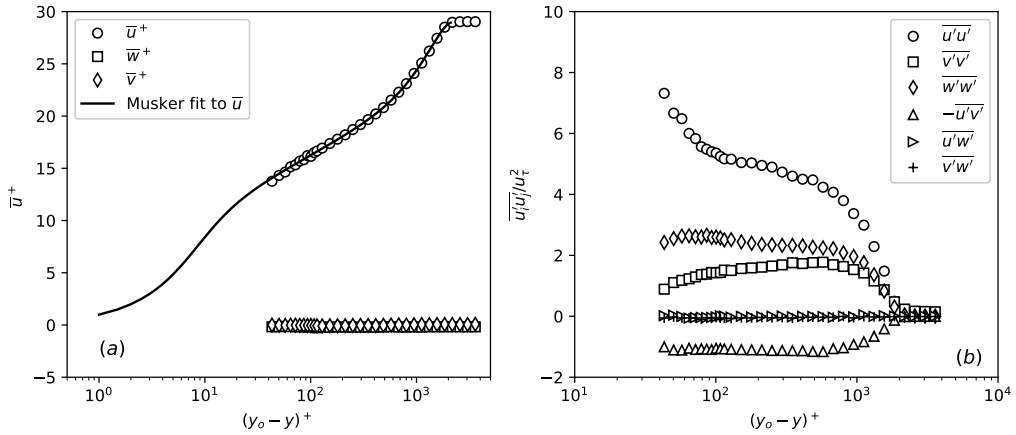


Figure 11. Measured boundary layer profile at $x = 1168.4$ mm, $z = 0$ mm for $\alpha = 0^\circ$. (a) Mean-velocity components and Musker fit in wall units. (b) Reynolds stresses in wall units.

Table 2. Boundary-layer parameters at $x = 1168.4$ mm, $z = 0$ mm for $\alpha = 0^\circ$

| | δ , mm | δ^* , mm | θ , mm | H | c_f | Re_θ | Π | ℓ_v , μm |
|-----------------------|---------------|-----------------|---------------|------|-----------------|-------------|-------|--------------------------|
| Experiment | 15.2 | 2.6 | 1.8 | 1.42 | 0.0024 | 7559 | 1.08 | 6.96 |
| FUN3D | 16.6 | 2.3 | 1.7 | 1.36 | 0.0027 | 7093 | 0.63 | 6.46 |
| ZPG TBL ³² | — | — | — | 1.33 | 0.0028 – 0.0027 | 7451 – 7599 | 0.55 | — |

fuselage surface location and is equal to -236.1 mm. Since this profile location is on a symmetry plane for $\alpha = 0^\circ$, the measured and computed \bar{w} velocity is zero, as are the Reynolds shear stresses, $\bar{u}'\bar{w}'$ and $\bar{v}'\bar{w}'$. The \bar{v} velocity across the boundary layer is also very small and the CFD agrees with the measurements to within the experimental uncertainty. In the outer region of the boundary layer, the measured \bar{u} velocity is in good agreement with CFD and both indicate a similar boundary layer thickness of approximately 16 mm. In the logarithmic region of the boundary layer, however, the measured \bar{u} velocity is shifted down relative to the CFD. This implies that the skin-friction coefficient at this location is lower for the experiment. In part, that difference may stem from the trip dots used to fix transition in the experiment, which introduce a momentum loss in the boundary layer that persists far downstream and that effect is not captured in the CFD.

When comparing the Reynolds normal stresses for the experiment to CFD (Fig. 10a), we see that the CFD overpredicts the $\bar{v}'\bar{v}'$ and $\bar{w}'\bar{w}'$ components and underpredicts the $\bar{u}'\bar{u}'$ component, with the largest deviation occurring near the wall. Those trends are typical of many RANS turbulent models, but the QCR2020 modification used in the present study was previously shown to offer significant improvements in the normal-stress predictions over earlier versions of QCR.¹² In contrast, the measured Reynolds shear-stress component $\bar{u}'\bar{v}'$ is predicted very well by the CFD.

Although the skin friction was not measured in the experiment, an estimate is desired so that several boundary-layer parameters at the $x = 1168.4$ mm location can be calculated and compared to CFD. To that end, an explicit closed form expression for the velocity distribution of a smooth wall turbulent boundary layer was least-squares fit to the \bar{u} velocity profile. This approach is reasonable given that the profile measurement was made on the symmetry plane of the flat fuselage side wall where the local boundary layer is essentially two dimensional at $\alpha = 0^\circ$. The expression for the velocity distribution, originally developed by Musker,³³ is parameterized by the friction velocity, u_τ , the boundary-layer thickness, δ , and the wake-strength parameter, Π . Using the friction velocity obtained from the curve fit, the wall shear stress and the skin-friction coefficient, c_f , were calculated. The curve fit was also used to calculate the integral properties of the boundary layer (i.e., the displacement thickness, δ^* , the momentum thickness, θ , and the shape factor, $H = \delta^*/\theta$), along with the momentum thickness Reynolds number, Re_θ , and the viscous length scale, $\ell_v = \nu/u_\tau$. These values are shown in Table 2 along with a companion set of parameter values from the FUN3D computations. As a point of reference, the values of H , c_f , and Π for a zero pressure gradient (ZPG) turbulent boundary layer are included in the table and those parameters were obtained from the tabulated values reported by Coles.³² Using the

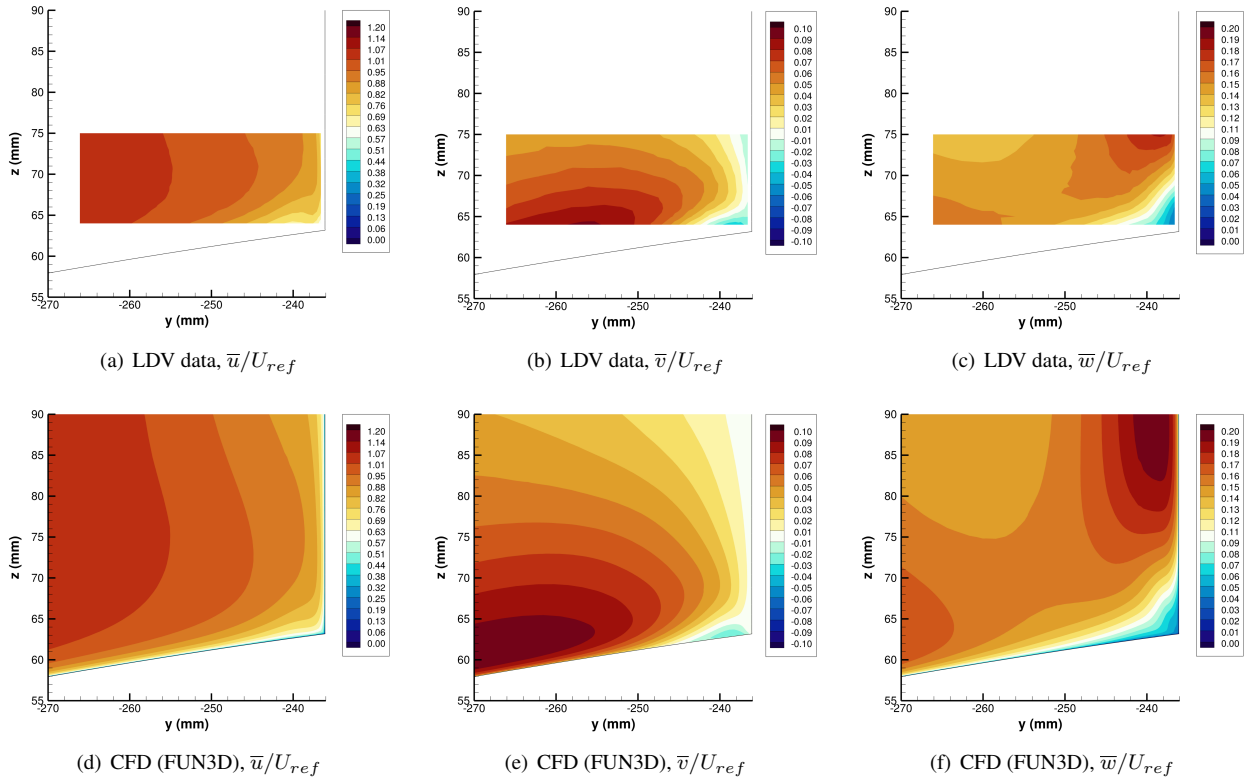


Figure 12. Contours of mean-velocity components at $x = 2145.0$ mm, $\alpha = 0^\circ$.

friction velocity from the curve fit, the boundary layer profile at $x = 1168.4$ mm is plotted with inner-layer scaling in Fig. 11. Here, the Musker curve fit is seen to provide a good correlation for the \bar{u} velocity profile.

The mean-velocity and Reynolds-stress profiles at the $x = 1861.5$ mm location are shown in Fig. 10b. Similar to the upstream profile, this location is on the symmetry plane, and therefore, the \bar{w} , $\bar{u}'\bar{w}'$, and $\bar{v}'\bar{w}'$ profiles are zero. The \bar{v} velocity is still small, but it is increasingly negative toward the edge of the boundary layer. This is due to the increased adverse pressure gradient and the resulting increased boundary-layer growth in the vicinity of the wing-fuselage junction. In the logarithmic region of the boundary layer, the measured \bar{u} velocity is again shifted down relative to the CFD. The two profile points closest to the wall also show a further deviation from the CFD, and this is due to spatial averaging across the LDV measurement volume in the high-gradient region of the near-wall flow. In terms of the Reynolds stresses, the CFD again overpredicts the $\bar{v}'\bar{v}'$ and $\bar{w}'\bar{w}'$ components and underpredicts the $\bar{u}'\bar{u}'$ component, but it provides a good prediction of the $\bar{u}'\bar{v}'$ component.

D. Mean-velocity and Reynolds-stress measurements in the wing-fuselage junction region

In this section, we focus the discussion on the y - z plane surveys that were made in the corner region of the wing-fuselage junction. The first location at $x = 2145$ mm ($x/c_r = 0.22$) was chosen to provide data on the early development of the corner flow. Contour plots of the measured and computed mean-velocity components, Reynolds normal stresses, and Reynolds shear stresses at this location are shown in Figs. 12, 13, and 14, respectively. Note that the survey region at this location was limited by the optical access provided by the fuselage window insert and that prevented us from positioning the LDV measurement volume along the downward sloping surface of the wing. Nevertheless, some important features of the corner flow can still be measured, particularly in the immediate vicinity of the corner.

Contours for the measured \bar{u} component (Fig. 12a) are locally distorted near the corner and above the wing surface, and this is due to secondary flow in the y - z plane. In particular, a close examination of the contours for the measured \bar{v} and \bar{w} components near the corner reveals that a corner vortex with clockwise rotation when looking upstream (negative streamwise vorticity) is responsible for the local lift up in the \bar{u} contours. The corresponding mean-velocity contours predicted with CFD are in good agreement with the measurements, showing similar mean-flow distortion

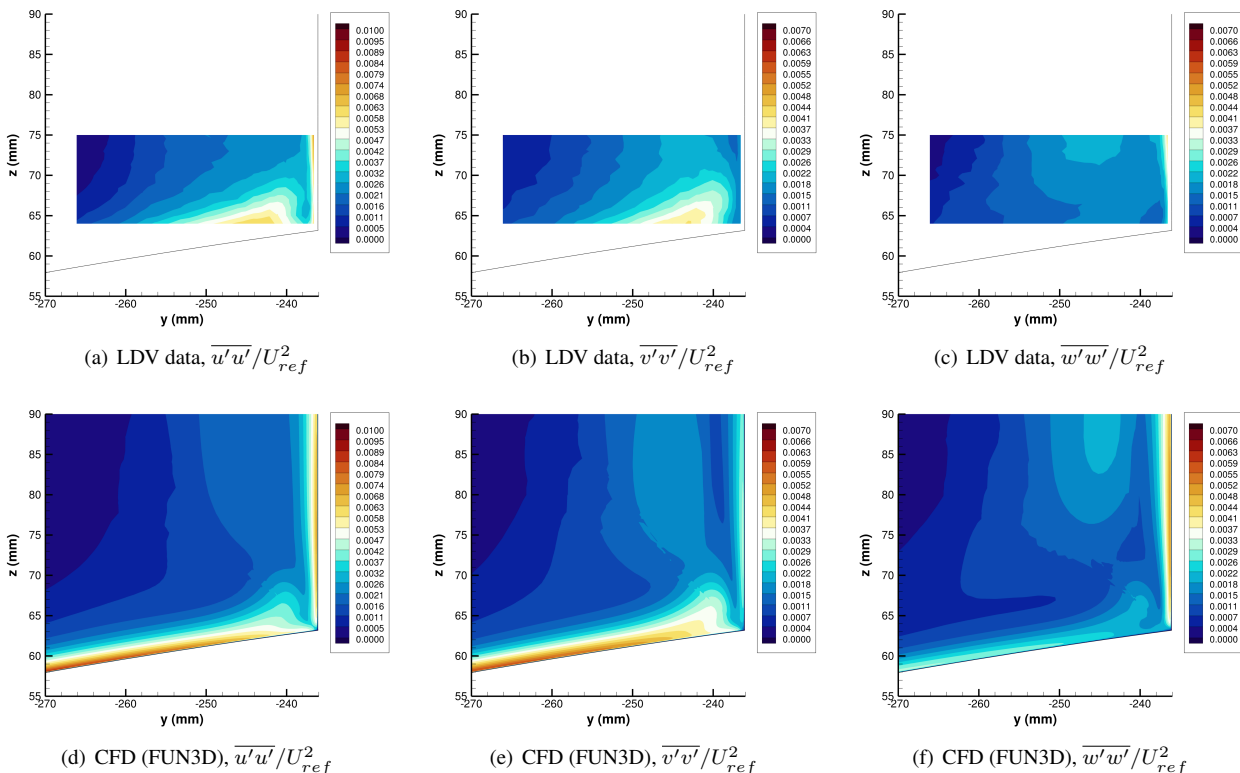


Figure 13. Contours of Reynolds normal stresses at $x = 2145.0$ mm, $\alpha = 0^\circ$.

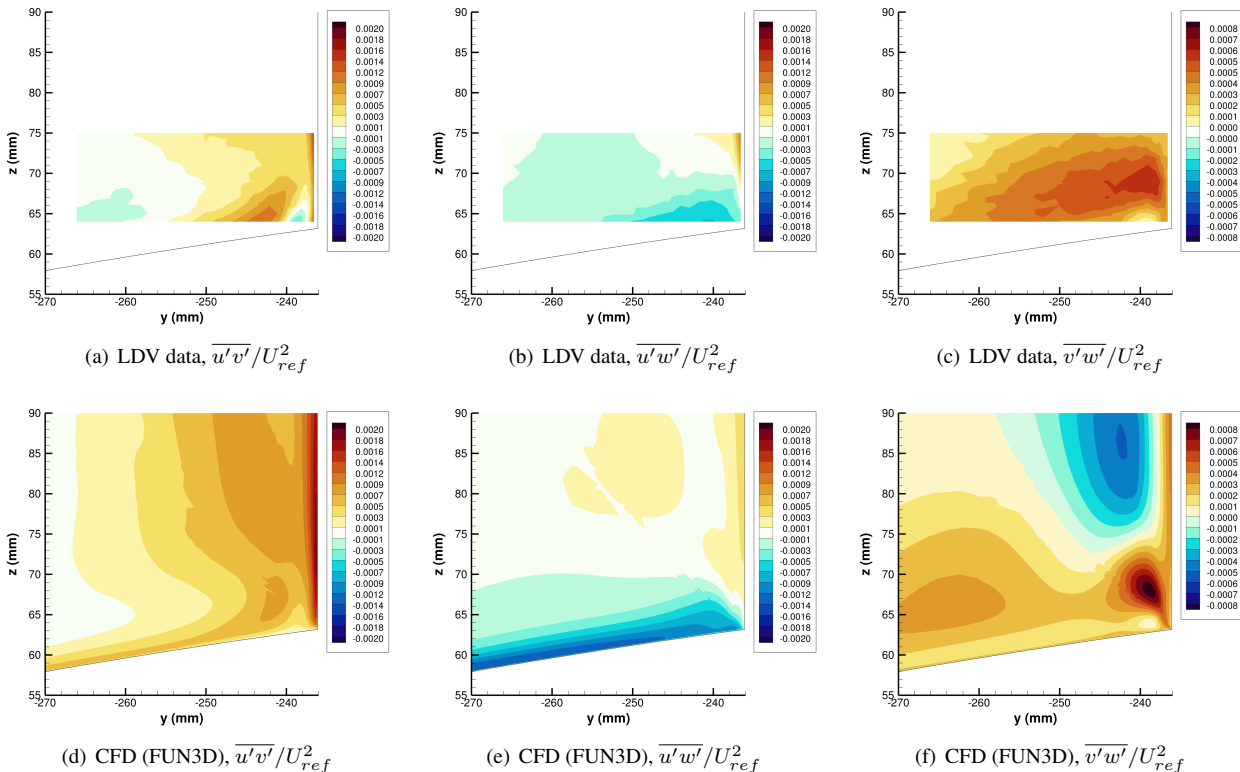


Figure 14. Contours of Reynolds shear stresses at $x = 2145.0$ mm, $\alpha = 0^\circ$.

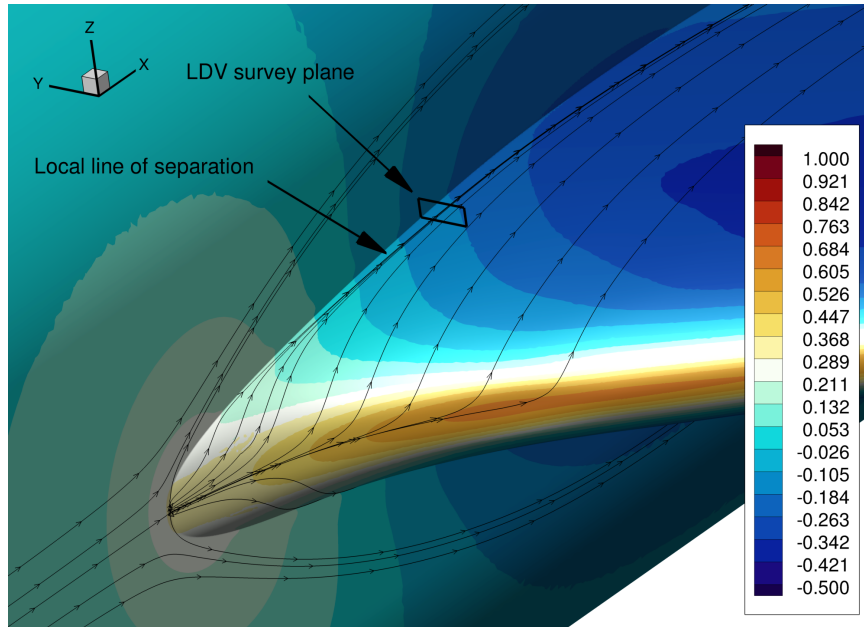


Figure 15. Computed surface pressure coefficient contours and skin-friction lines in the leading-edge region of the wing-fuselage junction at $\alpha = 0^\circ$.

in the \bar{u} component and a corner vortex associated with the secondary flow components \bar{v} and \bar{w} . Given the good agreement between the experiment and CFD, we can look to the computations for insight to the formation of the corner vortex. Figure 15 shows the computed surface pressure coefficient contours and skin-friction lines in the leading-edge region of the wing-fuselage junction. Very close to the leading-edge of the wing-fuselage junction, a nodal point of separation is predicted and almost immediately downstream, there is a nodal point of attachment. As such, a small region of separated flow is formed near the leading edge of the junction. Several skin-friction lines emanating from a small region near the nodal point of attachment are observed to bend inward, toward the corner, due to the pressure gradient on the leading-edge extension. Further downstream, those skin-friction lines converge onto a local line of separation. This line then serves as the base for a new stream surface (or dividing surface) that extends into the flow³⁴ and on passage downstream, the stream surface rolls up to form the corner vortex. It will be shown later in the discussion that this corner vortex persists downstream and extends all the way to the wing trailing edge.

In terms of the Reynolds-stress components, the predicted contours from CFD are generally in good qualitative agreement with the experiment. The contours for all three normal stresses are lifted up on the upwash side of the corner vortex and the $\bar{w}'\bar{w}'$ component, particularly along the wing surface, has a much lower magnitude than the $\bar{u}'\bar{u}'$ and $\bar{v}'\bar{v}'$ components. The experimental contours for the primary shear stress, $\bar{u}'\bar{v}'$, show a local maximum and minimum near the corner, on either side of the uplifted \bar{u} contours. In addition, there is a sign change in this shear stress associated with a sign change in $\partial\bar{u}/\partial y$ in that same region. While the CFD contours for this shear stress also display a local maximum and minimum, they do not display a sign change. A close inspection of the predicted \bar{u} contours shows that there is also no sign change in $\partial\bar{u}/\partial y$ across the uplifted region. The contours for the secondary shear stress, $\bar{v}'\bar{w}'$, exhibit the largest differences between the experiment and CFD, but it should be noted that this component has the largest experimental uncertainty. Nevertheless, in the immediate vicinity of the corner vortex, both the experimental and CFD contours display a local maximum and minimum in roughly the same locations.

Figure 16 shows the spatial evolution of selected mean-flow contours in the x direction near the wing trailing edge. Here, both measured data and CFD are compared and the x locations correspond to $x/c_r = 0.796, 0.966, 0.983$, and 0.999 . The \bar{u} contours (Fig. 16a) show the mean-flow distortion that occurs in the turbulent corner flow due to secondary flow in the y - z plane. They also show the overall deceleration of the corner flow due to the adverse pressure gradient imposed on the corner by the wing pressure distribution. The \bar{v} contours (Fig. 16c) show a couple of key features associated with the secondary flow. First, in the region away from the corner and along the wing surface, the secondary flow is moving away from the fuselage ($-\bar{v}$). In the region directly above, the secondary flow is moving toward the fuselage ($+\bar{v}$). That flow pattern is related to the corner vortex that was shown to form further upstream

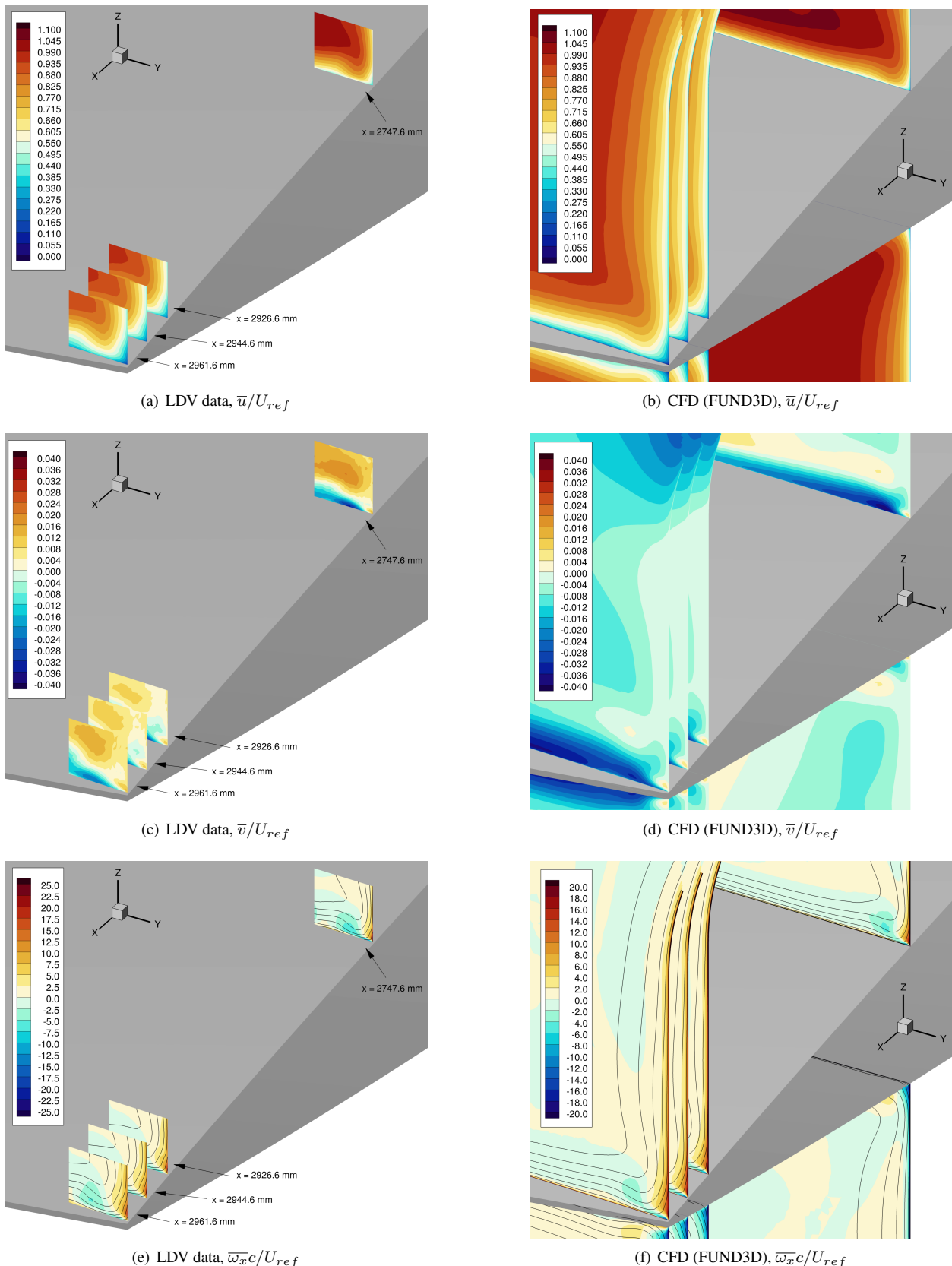


Figure 16. Progression of selected mean-flow contours of interest, $\alpha = 0.0^\circ$.

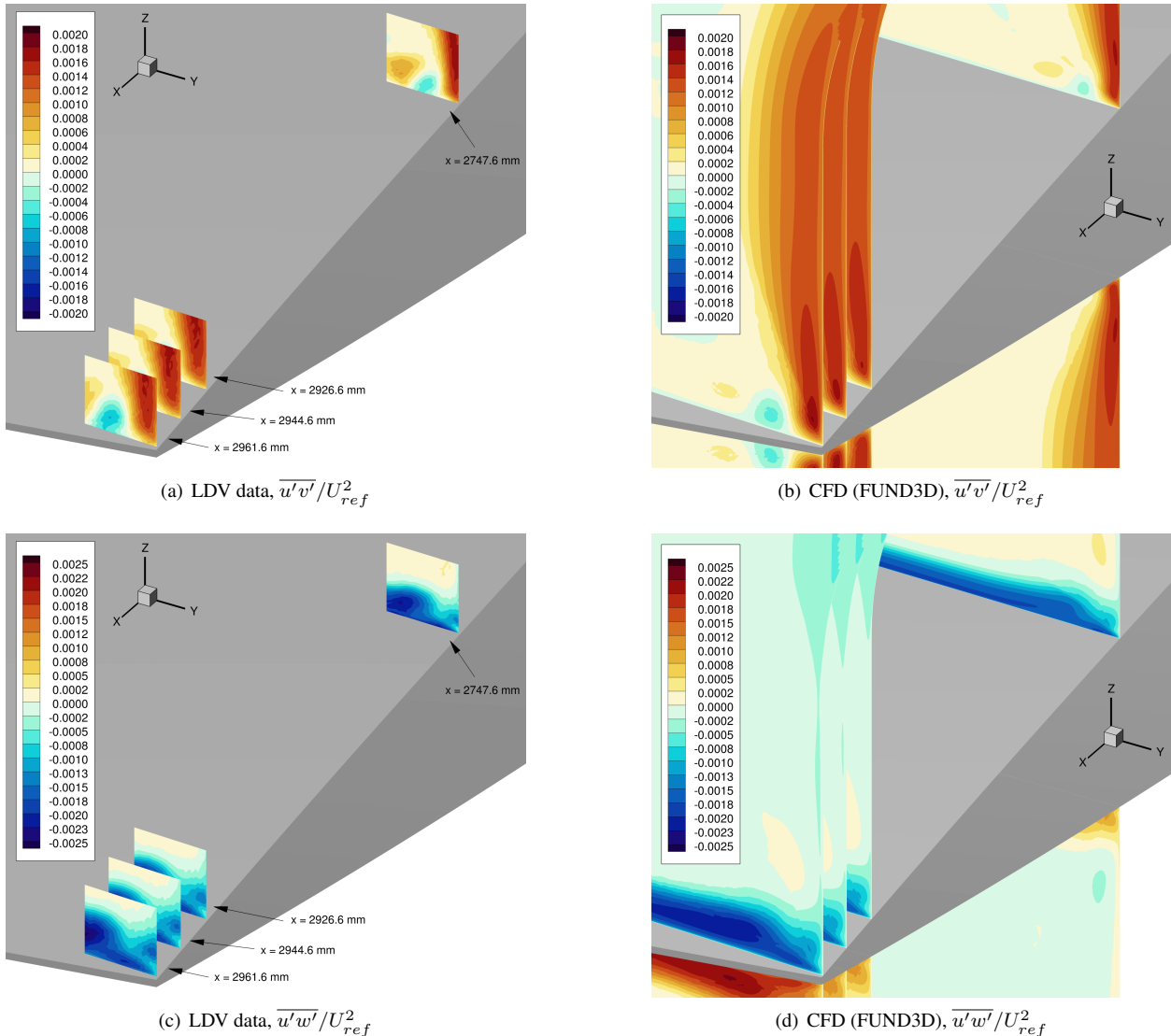


Figure 17. Progression of primary Reynolds shear stress contours, $\alpha = 0.0^\circ$.

during the early development of the corner flow. Second, in the immediate vicinity of the corner, there is a small region of secondary flow moving toward the corner and just above that, flow is moving away from the corner. That flow pattern is associated with a stress-induced vortex with counterclockwise rotation when looking upstream. This stress-induced vortex is a common feature of turbulent corner flows and arises from the production of streamwise vorticity by spatial gradients of the difference between the Reynolds normal stresses $\bar{v}'\bar{v}'$ and $\bar{w}'\bar{w}'$.¹¹ The $\bar{\omega}_x$ contours (Fig. 16e) show the mean streamwise vorticity associated with the secondary flow in the y - z plane. Here, there is a region of negative streamwise vorticity associated with the corner vortex and a region of positive streamwise vorticity associated with the stress-induced vortex deep in the corner.

The predicted mean-flow contours are generally in good agreement with the experiment and the similarities in the spatial distributions suggest that the turbulence model used for the computations (SA-RC-QCR2020) captures the essential flow physics of the turbulent corner flow. However, quantitative differences do exist. For example, the predicted secondary flow associated with the corner and stress-induced vortices is weaker and the streamwise vorticity is somewhat less than the experimental data. Since the strength of the stress-induced vortex is expected to play a role in the onset of corner separation, these differences may partly explain why a small corner-flow separation is predicted, while the experiment indicates fully attached corner flow for $\alpha = 0^\circ$ (see the earlier discussion in Section IV.A).

Figure 17 shows the spatial evolution of the primary Reynolds shear-stress contours ($\bar{u}'\bar{v}'$ and $\bar{u}'\bar{w}'$) in the x direction. As before, both measured data and CFD are compared and the x locations are the same. The contours show

that $\overline{u'v'}$ is the dominant shear stress in the fuselage boundary layer, while $\overline{u'w'}$ is the dominant shear stress in the wing boundary layer, as expected. The secondary flow produced by the corner and stress-induced vortices—along with the associated mean-flow distortion in \bar{u} —leads to the complex distributions that are observed for $u'v'$ and $u'w'$ in the corner region. Overall, the predicted primary shear-stress components are in very good agreement with the experimental data.

To provide a quantitative comparison between the experimental data and CFD, mean-velocity and Reynolds-stress profiles are shown in Fig. 18 for an x location of 2837.1 mm ($x/c_r = 0.881$). As with the fuselage profiles shown earlier, the symbols denote the experimental data, the solid lines denote CFD predictions, and the shaded bands about the experimental data represent the measurement uncertainty. The profiles were obtained from flowfield surveys in the z direction at three spanwise locations. The first location at $y = -239.1$ mm is deep within the fuselage boundary layer and cuts through the stress-induced vortex, the second location at $y = -246.1$ mm is influenced by the downwash of the corner vortex, and the third location at $y = -266.1$ mm is near or just outboard of the upwash region produced by the corner vortex. In terms of the mean-velocity components, the overall agreement between the experimental data and CFD is good, but small quantitative differences—larger than the measurement uncertainty—can be observed. Similar to the boundary-layer measurements on the fuselage, the predicted normal-stress components $\overline{v'v'}$ and $\overline{w'w'}$ are overpredicted (although not significantly) and $\overline{u'u'}$ is underpredicted relative to the experimental data. However, there is still good qualitative agreement between experiment and CFD for all three spanwise locations. The predicted shear-stress profiles show varying levels of agreement with the experimental data and overall, qualitatively capture the experimental distributions.

Next, we examine the flowfield contours at two x locations in more detail. The first location is at $x = 2747.6$ mm ($x/c_r = 0.796$) and contours for the mean-velocity components, the Reynolds normal stresses, and the Reynolds shear stresses are shown in Figs. 19, 20, and 21, respectively. As discussed earlier, the mean flow distortion in \bar{u} (Fig. 19a) is due to the secondary flow produced by the corner vortex and the stress-induced vortex. The corner vortex produces the lift up in the \bar{u} contours along the wing surface and on the upwash side of the vortex, while the \bar{u} contours are driven down toward the wing surface on the downwash side, producing a fuller boundary-layer profile. Near the wing-fuselage corner, the stress-induced vortex (with counterclockwise rotation) causes the \bar{u} contours to bend slightly away from the fuselage surface. The predicted mean-flow contours are in good agreement with the experiment, but it is clear that the predicted secondary flow is weaker in some regions of the flowfield and the mean-flow distortion in \bar{u} is somewhat less. For the normal stresses (Fig. 20), all three components are intensified on the upwash side of the corner vortex and attenuated deep in the wing-fuselage corner. Along the wing surface, the $\overline{w'w'}$ component is generally weaker than the $\overline{v'v'}$ component due to the constraining effect of the wall. Along the fuselage surface, the opposite is true. The same patterns are observed in the predicted normal-stress contours, but as previously discussed, the CFD consistently underpredicts the $\overline{u'u'}$ component and overpredicts the $\overline{v'v'}$ and $\overline{w'w'}$ components. In particular, the strong enhancement in the $\overline{u'u'}$ component on the upwash side of the corner vortex is not captured in the CFD. Similar to the normal stresses, the shear-stress components $\overline{u'v'}$ and $\overline{u'w'}$ (Fig. 21) are enhanced on the upwash side of the corner vortex. The predicted shear-stress contours are in relatively good agreement with the experimental data, showing similar flowfield patterns. However, the predicted $\overline{u'v'}$ and $\overline{u'w'}$ components are slightly weaker and the secondary shear-stress component $\overline{v'w'}$ is slightly stronger than the experimental data.

Finally, we examine the flowfield contours at $x = 2961.6$ mm ($x/c_r = 0.999$), which is just upstream of the wing trailing edge. The mean-flow components, the Reynolds normal stresses, and the Reynolds shear stresses for this location are shown in Figs. 22, 23, and 24, respectively. Most of the comments made for the upstream location apply here as well. The main differences are that the fuselage and wing boundary layers are significantly thicker, the mean flow is decelerated, and the corner vortex has migrated further outboard, in part due to the spanwise pressure gradient of the swept wing and the induced motion from the vortex image.

V. Summary

In this paper, we reported on a third test campaign with the NASA Juncture Flow model in the 14x22 wind tunnel. The overall objective of this test was to expand the existing Juncture Flow CFD Validation data set with a symmetric-wing configuration that displayed a progression from fully attached corner flow to separated corner flow near the trailing edge of the wing-fuselage junction, depending on the model angle of incidence. The newly developed data set includes detailed LDV measurements at three model angles of incidence corresponding to fully attached corner flow ($\alpha = 0^\circ$), incipient corner-flow separation ($\alpha = 1^\circ$), and separated corner flow ($\alpha = 5^\circ$). For each angle, the LDV data set consists of profile surveys at several locations on the fuselage and y - z planar surveys at several x locations along the wing-fuselage junction. Supporting measurements in the form of model static pressures, tunnel wall static

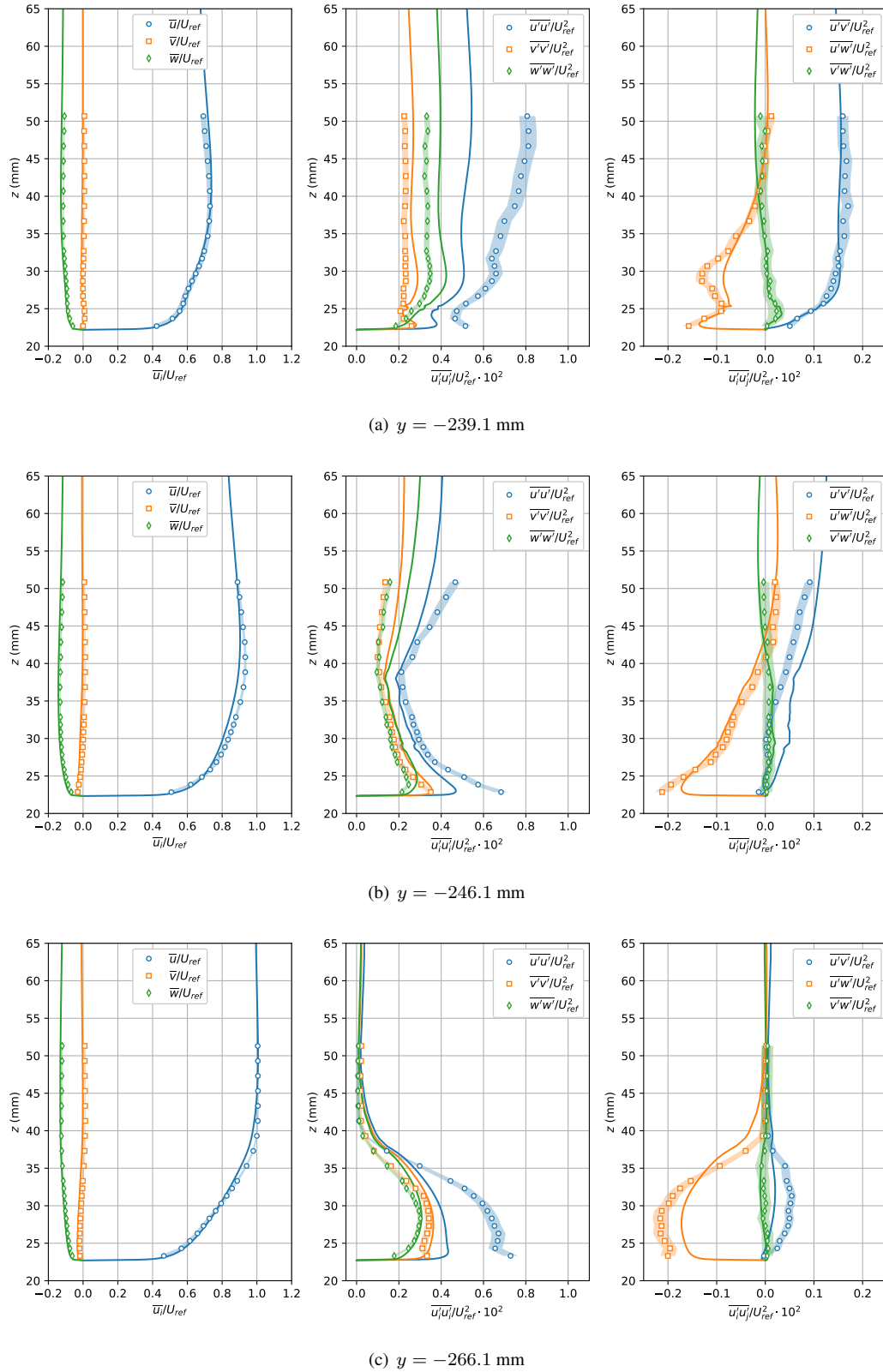


Figure 18. Measured (symbols) and computed (lines) mean-velocity and Reynolds-stress profiles at $x = 2837.1 \text{ mm}$ and $\alpha = 0^\circ$.

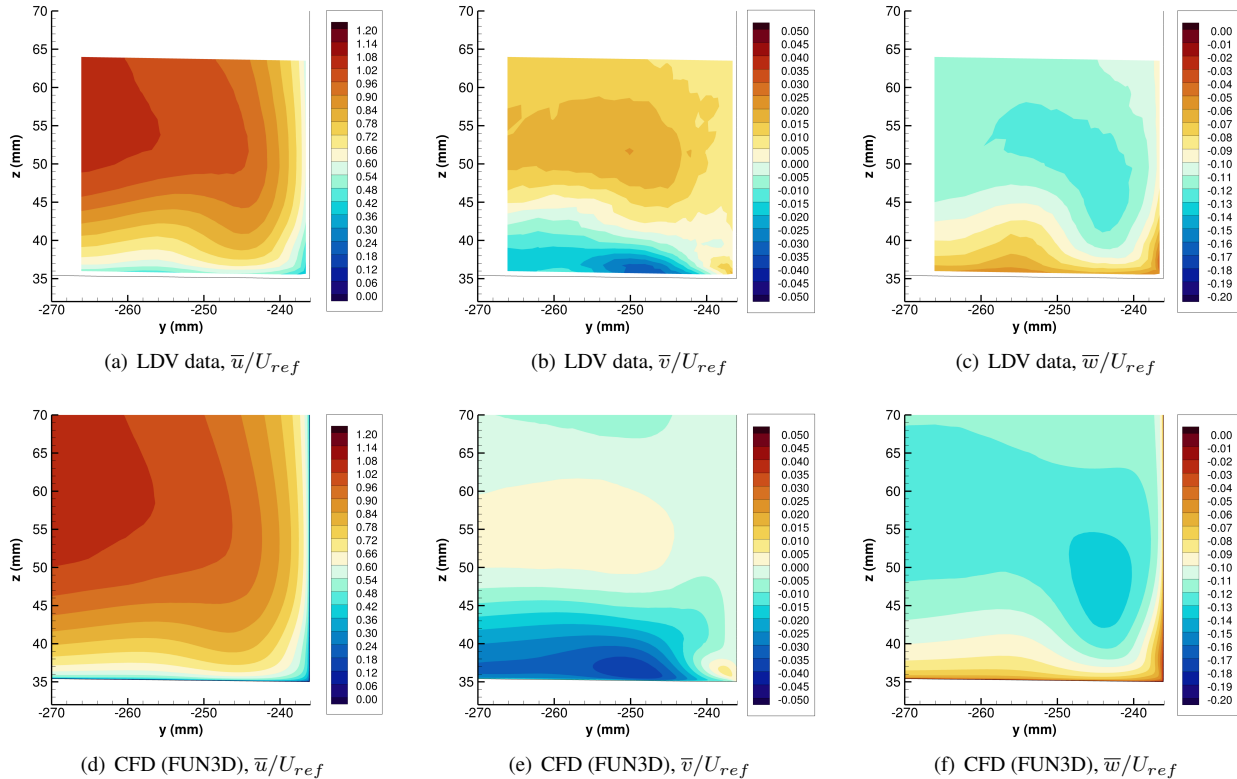


Figure 19. Contours of mean-velocity components at $x = 2747.6$ mm, $\alpha = 0^\circ$.

pressures, tunnel wall and ceiling boundary-layer-rake pressures, oil-flow visualizations in the wing-fuselage junction region, and laser-based measurements of the as-built geometry and model position in the test section are included in the data set. All data from this test entry are available on the NASA Langley Turbulence Modeling Resource website.¹⁰

A sampling of the results from the test entry were presented and the discussion was focused on the fully attached corner flow case at $\alpha = 0^\circ$. From the LDV measurements, two key features of the turbulent corner flow were revealed. First, in the early development of the corner flow, just downstream of the wing root leading edge, a corner vortex with clockwise rotation (when looking upstream) forms. As this vortex travels downstream, it slowly migrates outboard. But even as it approaches the wing trailing edge, it remains relatively close to the corner and exerts an influence on the turbulent corner flow. Second, at a somewhat later point in the corner-flow development, a stress-induced vortex with counterclockwise rotation (when looking upstream) forms deep in the corner of the wing-fuselage junction and persists all the way to the junction trailing edge. This vortex brings momentum into the corner and helps to keep the flow attached there as it progresses through the adverse pressure gradient imposed on the corner by the wing.

Computations for the experimental test case were performed with FUN3D using SA-RC with the recently developed QCR2020 modification. Overall, this turbulence model performs very well in comparison to the experimental data set. In terms of the model C_p distributions, the CFD was in very good quantitative agreement with the experimental data. In terms of the flowfield quantities (both mean-flow components and Reynolds stresses) the CFD was generally in very good qualitative agreement, displaying spatial distributions there were similar to the experimental data. For profiles on the fuselage, differences in the mean flow between CFD and experiment may be attributed to the way in which boundary-layer transition on the fuselage nose is imposed in the computations. In the wing-fuselage junction region, the good qualitative agreement in both the mean-flow components and the Reynolds stresses suggests that the turbulence model is capturing the essential flow physics. In particular, both the corner vortex and the stress-induced vortex are predicted by the CFD. However, quantitative differences between the CFD and experimental data do exist. The CFD consistently underpredicts the $u'u'$ component and overpredicts the $v'v'$ and $w'w'$ components in all of the measurements locations considered. For the fuselage boundary layer, these mispredictions may not be too critical, but they are more important in the wing-fuselage corner-flow region. There, gradients in the difference between $v'v'$ and $w'w'$ produce mean streamwise vorticity. As such, a misprediction in those quantities will effect the strength of the secondary flow. That is particularly important deep in the corner where the resulting stress-induced

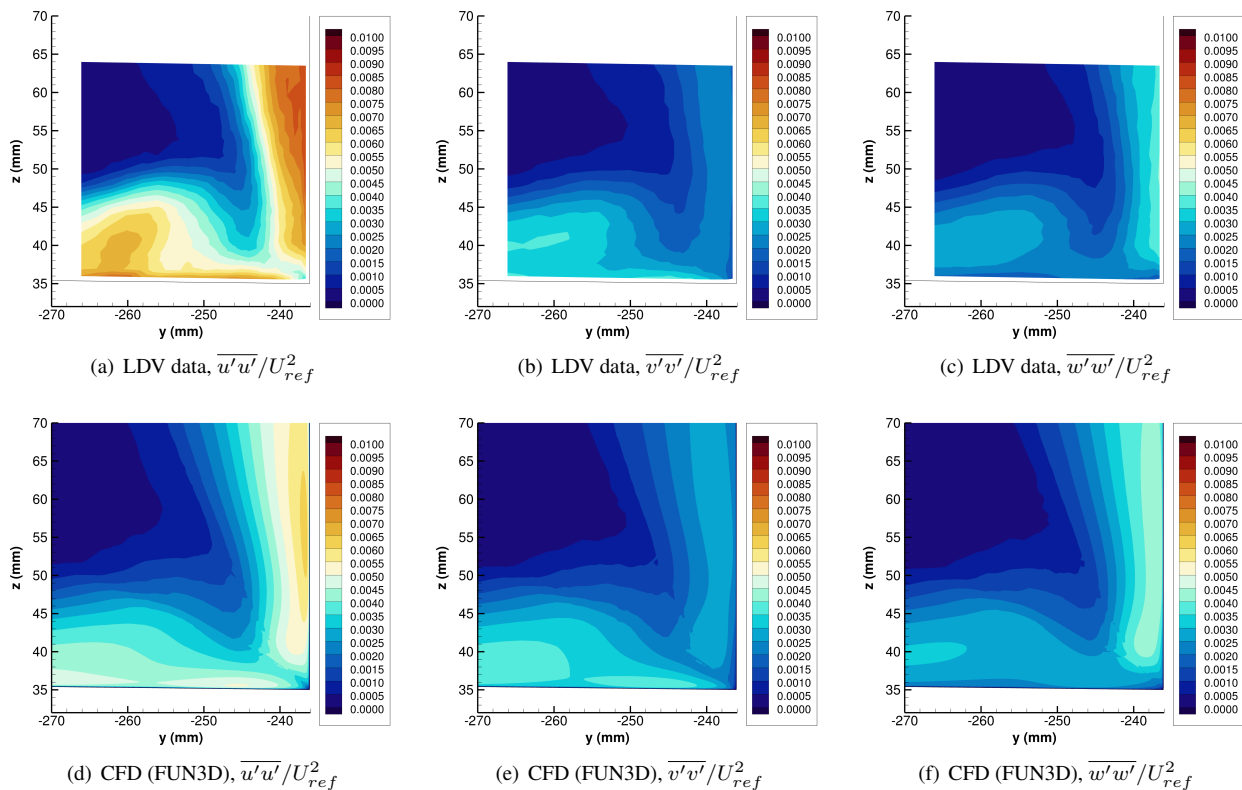


Figure 20. Contours of Reynolds normal stresses at $x = 2747.6$ mm, $\alpha = 0^\circ$.

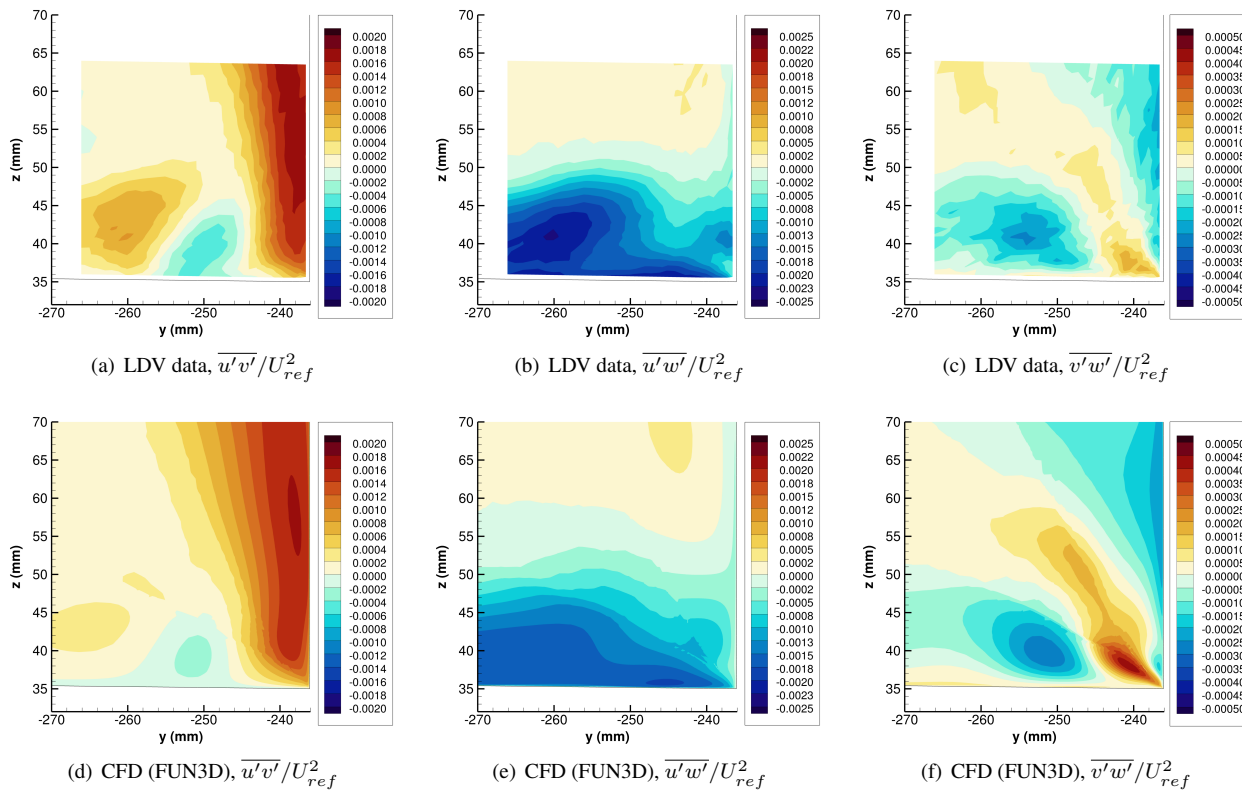


Figure 21. Contours of Reynolds shear stresses at $x = 2747.6$ mm, $\alpha = 0^\circ$.

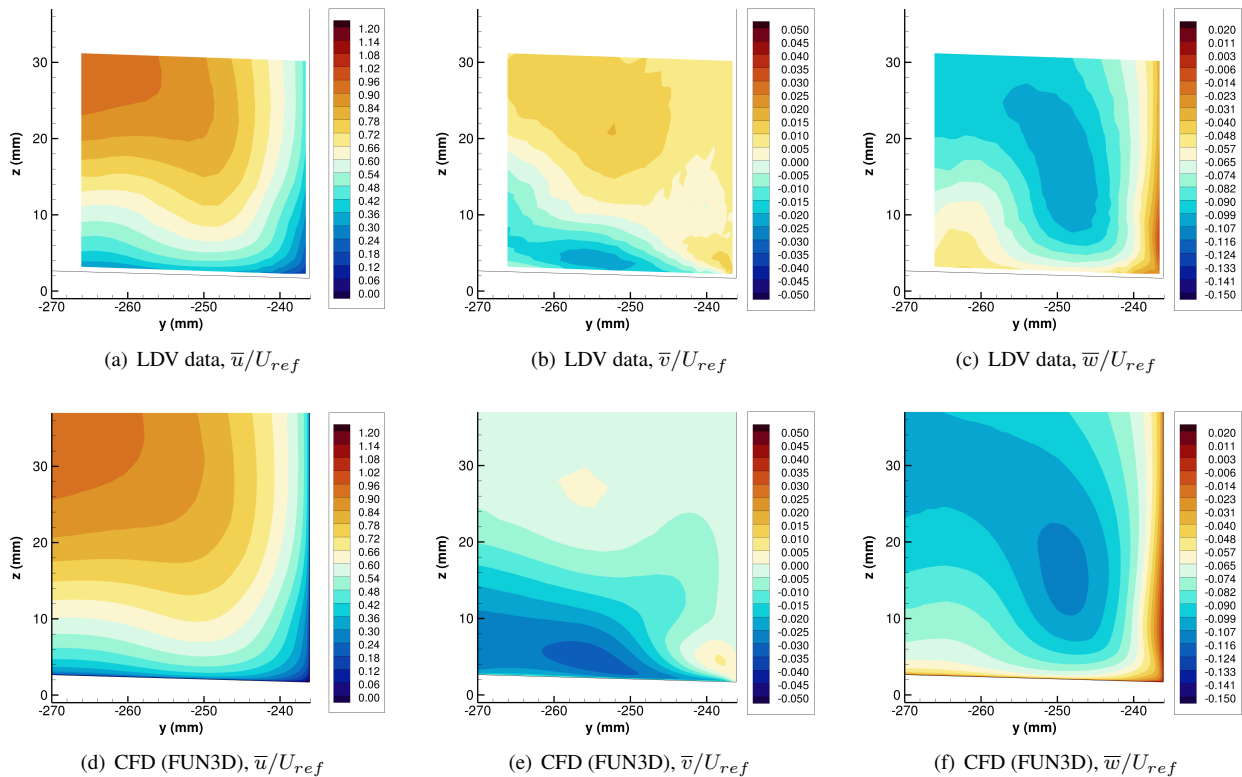


Figure 22. Contours of mean-velocity components at $x = 2961.6$ mm, $\alpha = 0^\circ$.

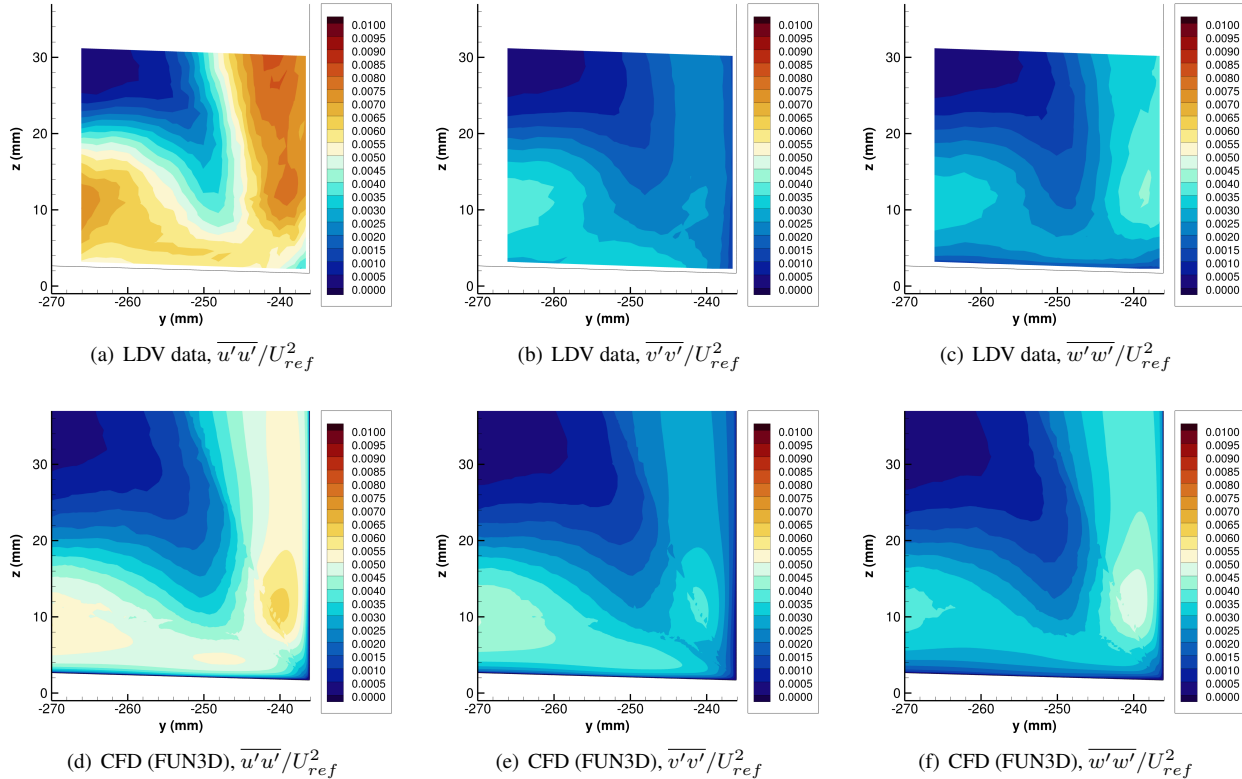


Figure 23. Contours of Reynolds normal stresses at $x = 2961.6$ mm, $\alpha = 0^\circ$.

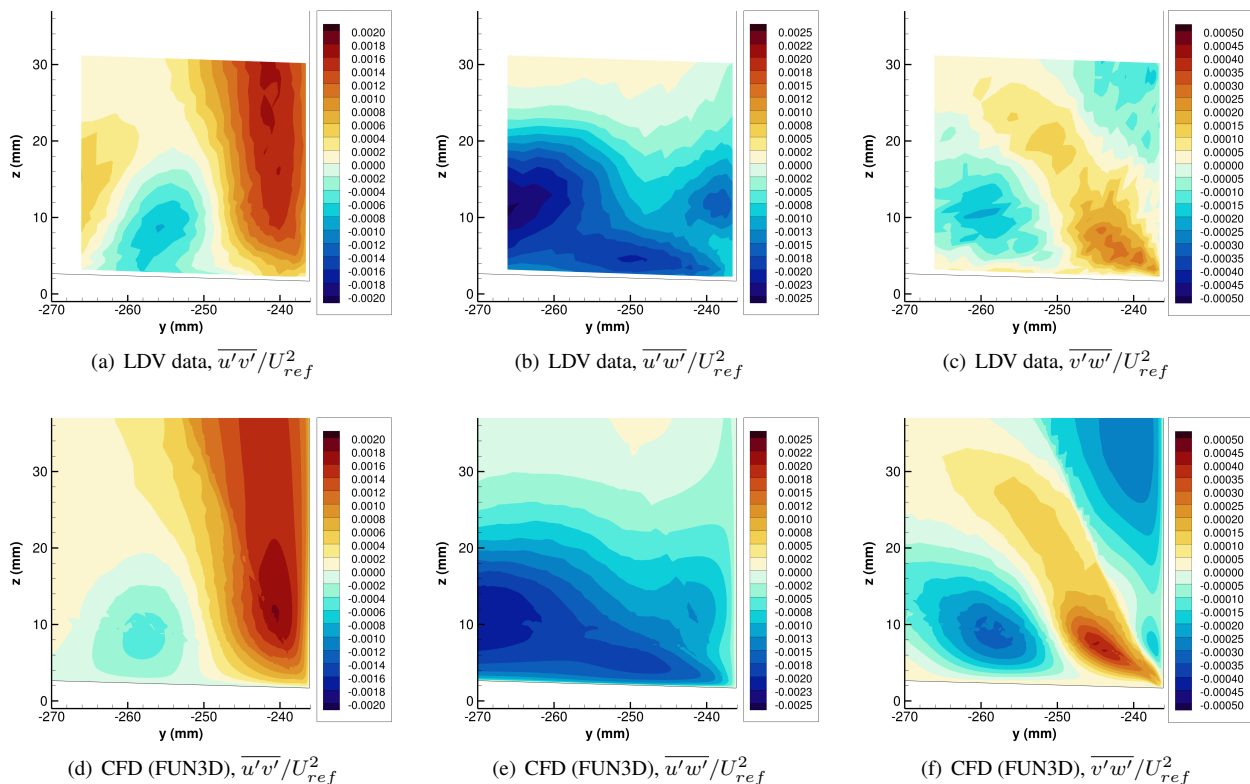


Figure 24. Contours of Reynolds shear stresses at $x = 2961.6$ mm, $\alpha = 0^\circ$.

vortex plays a key role in the onset of corner-flow separation. In fact, the predicted secondary flow in the corner was found to be slightly weaker than the experimental data and that may explain why the CFD predicts a small corner-flow separation while the experimental data indicates fully attached corner flow for the $\alpha = 0^\circ$ test case.

Acknowledgements

This work was supported by the NASA Transformational Tools and Technologies project of the Transformative Aeronautics Concepts Program. The authors thank all members of the Juncture Flow Team for their dedication and insights throughout the course of this effort. The authors would also like to thank the staff of the 14- by 22-Foot Subsonic Tunnel for their support during the test entry.

References

- ¹Mauery, T., Alonso, J., Cary, A., Lee, V., Malecki, R., Mavriplis, D., Medic, G., Schaefer, J., and Slotnick, J., “A Guide for Aircraft Certification by Analysis,” NASA CR 20210015404, May 2021.
- ²Rumsey, C. L., Neuhart, D. H., and Kegerise, M. A., “The NASA Juncture Flow Experiment: Goals, Progress, and Preliminary Testing,” AIAA Paper 2016-1557, January 2016.
- ³Kegerise, M. A. and Neuhart, D. H., “An Experimental Investigation of a Wing-Fuselage Junction Model in the NASA Langley 14- by 22-Foot Subsonic Tunnel,” NASA TM 2019-220286, June 2019.
- ⁴Kegerise, M. A., Neuhart, D. H., Hannon, J. A., and Rumsey, C. L., “An Experimental Investigation of a Wing-Fuselage Junction Model in the NASA Langley 14- by 22-Foot Subsonic Wind Tunnel,” AIAA Paper 2019-0077, January 2019.
- ⁵Rumsey, C. L., Ahmad, N. N., Carlson, J. R., Kegerise, M. A., Neuhart, D. H., Hannon, J. A., Jenkins, L. N., Yao, C. S., Balakumar, P., Gildersleeve, S., Bartarm, S. M., Pulliam, T. H., Olsen, M. E., and Spalart, P. R., “NASA Juncture Flow Computational Fluid Dynamics Validation Experiment,” *AIAA Journal*, Vol. 60, No. 8, 2022, pp. 4789–4805.
- ⁶Taylor, N. J. and Rumsey, C. L., “CFD Validation Experiments: Toward a Broader Perspective,” AIAA Paper 2021-1933, January 2021.
- ⁷Brodersen, O. and Stürmer, A., “Drag Prediction of Engine-Airframe Interference Effects Using Unstructured Navier-Stokes Calculations,” AIAA Paper 2001-2414, June 2001.
- ⁸Jenkins, L. N., Yao, C. S., and Bartram, S. M., “Flow-Field Measurements in a Wing-Fuselage Junction Using an Embedded Particle Image Velocimetry System,” AIAA Paper 2019-0078, January 2019.

- ⁹Rumsey, C. L., Carlson, J. R., Hannon, J. A., Jenkins, L. N., Bartram, S. M., Pulliam, T. H., and Lee, H. C., "Boundary Condition Study for the Juncture Flow Experiment in the NASA Langley 14x22-Foot Subsonic Wind Tunnel," AIAA Paper 2017-4126, June 2017.
- ¹⁰Rumsey, C. L., "NASA Langley Turbulence Modeling Resource Website," <https://turbmodels.larc.nasa.gov> Accessed: 2022-08-05.
- ¹¹Perkins, H. J., "The Formation of Streamwise Vorticity in Turbulent Flow," *Journal of Fluid Mechanics*, Vol. 44, 1970, pp. 721–740.
- ¹²Rumsey, C. L., Carlson, J. R., Pulliam, T. H., and Spalart, P. R., "Improvements to the Quadratic Constitutive Relation Based on NASA Juncture Flow Data," *AIAA Journal*, Vol. 58, No. 10, October 2020, pp. 4374–4384.
- ¹³Kuester, M. S., Borgoltz, A., and Devenport, W. J., "Experimental Visualization of Juncture Separation Bubbles at Low- to Moderate-Reynolds Numbers," AIAA Paper 2016-3880, June 2016.
- ¹⁴Kegerise, M. A. and Neuhart, D. H., "Wind Tunnel Test of a Risk-Reduction Wing/Fuselage Model to Examine Juncture-Flow Phenomena," NASA TM 219348, 2016.
- ¹⁵Leidy, A. N., Kegerise, M. A., Hannon, J. A., Choudhari, M., Venkatachari, B., and Paredes, P., "Measurements and Computations of Natural Transition on the NASA Juncture-Flow Model with a Symmetric Wing," AIAA Paper 2023-xxxx, January 2023.
- ¹⁶Neuhart, D. H. and McGinley, C. B., "Free-Stream Turbulence Intensity in the Langley 14- by 22-Foot Subsonic Tunnel," NASA TP 213247, 2004.
- ¹⁷Gentry, G. L., Quinto, F. P., Gatlin, G. G., and Applin, Z. T., "The Langley 14- by 22-Foot Subsonic Tunnel," NASA TP 3008, 1990.
- ¹⁸Lowe, K. T., *Design and Application of a Novel Laser-Doppler Velocimeter for Turbulence Structural Measurements in Turbulent Boundary Layers*, Phd thesis, Virginia Polytechnic Institute and State University, Blacksburg, VA, September 2006.
- ¹⁹Lowe, K. T. and Simpson, R. L., "An Advanced Laser-Doppler Velocimeter for Full-Vector Particle Position and Velocity Measurements," *Meas. Sci. Technol.*, Vol. 20, 2009, pp. 1–16.
- ²⁰Brooks, D. R. and Lowe, K. T., "Development and Application of a Compact Spatially Resolving Vector Laser Velocimeter for Near Surface Flow Measurements," *16th Int. Symp. on Applications of Laser Techniques to Fluid Mechanics*, Lisbon, Portugal, 2012.
- ²¹Ölçmen, S. M. and Simpson, R. L., "An Experimental Study of a Three-Dimensional Pressure-Driven Turbulent Boundary Layer," *Journal of Fluid Mechanics*, Vol. 290, 1995, pp. 225–262.
- ²²Albrecht, H. E., Borys, M., Damaschke, N., and Tropea, C., *Laser Doppler and Phase Doppler Measurement Techniques*, Springer, Berlin, Germany, 2003.
- ²³Aeschliman, D. P. and Oberkampf, W. L., "Experimental Methodology for Computational Fluid Dynamics Code Validation," *AIAA Journal*, Vol. 36, No. 5, May 1998, pp. 733–741.
- ²⁴Anderson, W. and Bonhaus, D., "An Implicit Upwind Algorithm for Computing Turbulent Flows on Unstructured Grids," *Computers and Fluids*, Vol. 23, No. 1, 1994, pp. 1–22.
- ²⁵Anderson, W., Rausch, R., and Bonhaus, D. L., "Implicit/Multigrid Algorithms for Incompressible Turbulent Flows on Unstructured Grids," *Journal of Computational Physics*, Vol. 128, 1996, pp. 391–408.
- ²⁶Roe, P. L., "Approximate Riemann Solvers, Parameter Vectors, and Difference Schemes," *Journal of Computational Physics*, Vol. 43, 1981, pp. 357–372.
- ²⁷"FUN3D User's Manual," <https://fun3d.larc.nasa.gov> Accessed: 2022-08-25.
- ²⁸Rumsey, C. L., Lee, H. C., and Pulliam, T. H., "Reynolds-Averaged Navier-Stokes Computations of the NASA Juncture Flow Model Using FUN3D and OVERFLOW," AIAA Paper 2020-1304, January 2020.
- ²⁹Ahmad, N. N., Rumsey, C. L., and Carlson, J. R., "In-Tunnel Simulations of the NASA Juncture Flow Model," AIAA Paper 2021-1428, January 2021.
- ³⁰Spalart, P. R. and Allmaras, S. R., "A One-Equation Turbulence Model for Aerodynamic Flows," *Recherche Aerospatiale*, Vol. 1, 1994, pp. 5–21.
- ³¹Shur, M. L., Strelets, M. K., Travin, A. K., and Spalart, P. R., "Turbulence Modeling in Rotating and Curved Channels: Assessing the Spalart-Shur Correction," *AIAA Journal*, Vol. 38, No. 5, 2000, pp. 784–792.
- ³²Coles, D. E., "The turbulent boundary layer in a compressible flow," RAND Report R-403-PR, September 1962.
- ³³Musker, A. J., "Explicit Expression for the Smooth Wall Velocity Distribution in a Turbulent Boundary Layer," *AIAA Journal*, Vol. 17, No. 6, June 1979, pp. 655–657.
- ³⁴Tobak, M. and Peake, D. J., "Topology of Three-Dimensional Separated Flows," *Annual Review of Fluid Mechanics*, Vol. 14, 1982, pp. 61–85.